Key Points:
- Bathymetric and real-time hydroacoustic monitoring took place during the 2011–2012 El Hierro submarine eruption and the seafloor was later imaged and sampled in situ by remote operated vehicle ROV
- A new submarine volcano named Tagoro was built over two main episodes intercalated with collapse events, with eruptive activity ranging from effusive to explosive with a wide range of eruption styles and associated products, even over short time intervals
- Products include volcaniclastic aprons, glassy ash and lapilli, lava balloons, lava ponds, bulbous pillow lavas, scoria, and hydrothermal hornitos

Evolution of submarine eruptive activity during the 2011–2012 El Hierro event as documented by hydroacoustic images and remotely operated vehicle observations

L. Somoza[1] , F. J. González[1] , S. J. Barker[2] , P. Madureira[3] , T. Medialdea[1] , C. de Ignacio[4] , N. Lourenço[5] , R. León[1] , J. T. Vázquez[6] , and D. Palomino[6]

[1]Marine Geology Dv., Geological Survey of Spain (IGME), Madrid, Spain, [2]School of Environment, University of Auckland, Auckland, New Zealand, [3]Estrutura de Missão para a Extensão da Plataforma Continental, Portugal/Dpt. Geociências e ICT, Univ. Évora, R. Romão Ramalho, Portugal, [4]Petrology Dpt., Facultad Ciencias Geológicas, Universidad Complutense, Madrid, Spain, [5]Instituto Português do Mar e da Atmosfera, Lisboa, Portugal, [6]Instituto Español de Oceanografía, Fuengirola, Málaga, Spain

Abstract Submarine volcanic eruptions are frequent and important events, yet they are rarely observed. Here we relate bathymetric and hydroacoustic images from the 2011 to 2012 El Hierro eruption with surface observations and deposits imaged and sampled by ROV. As a result of the shallow submarine eruption, a new volcano named Tagoro grew from 375 to 89 m depth. The eruption consisted of two main phases of edifice construction intercalated with collapse events. Hydroacoustic images show that the eruptions ranged from explosive to effusive with variable plume types and resulting deposits, even over short time intervals. At the base of the edifice, ROV observations show large accumulations of lava balloons changing in size and type downslope, coinciding with the area where floating lava balloon fallout was observed. Peaks in eruption intensity during explosive phases generated vigorous bubbling at the surface, extensive ash, vesicular lapilli and formed high-density currents, which together with periods of edifice gravitational collapse, produced extensive deep volcaniclastic aprons. Secondary cones developed in the last stages and show evidence for effusive activity with lava ponds and lava flows that cover deposits of stacked lava balloons. Chaotic masses of heterometric boulders around the summit of the principal cone are related to progressive sealing of the vent with decreasing or variable magma supply. Hornitos represent the final eruptive activity with hydrothermal alteration and bacterial mats at the summit. Our study documents the distinct evolution of a submarine volcano and highlights the range of deposit types that may form and be rapidly destroyed in such eruptions.

Plain Language Summary Today and through most of geological history, the greatest number and volume of volcanic eruptions on Earth have occurred underwater. However, in comparison to subaerial eruption, little is known about submarine eruptive processes as they are dangerous to cruise it over, especially during explosive phases. This work shows the results of a study carried out during the eruption of the submarine volcano occurred during 2011–2012 1 km offshore El Hierro Island, Canary Islands, Spain. The submarine volcano emitted periodically large bubbles of gas, ashes, and giant steamed lava balloons that floated in the sea surface before sinking. These products identified later after the eruption using a submersible vehicle forming huge accumulations of lava balloons on the seafloor. More quiet periods erupted toothpaste lava from secondary cones which formed stalactite-like formations. Massive accumulation of blocks on the summit evidence intermittent violent explosions occurred when the cooling of lava progressively close the vent accumulating gas that finally exploded. The final stage of this submarine eruption consisted in the formation of chimneys by liquid-like lavas mixed with hydrothermal fluids forming 5-10 m tall "hornitos" structures at the summit of the volcano at 89 m depth but without emerging as it was expected.

1. Introduction

Today and through most of geological history, the greatest number and volume of volcanic eruptions on Earth have occurred underwater along mid-ocean ridges, near subduction zones, on oceanic plateaus, and on thousands of intraplate seamounts [*Rubin et al.*, 2012]. However, in comparison to their subaerial equivalents, little
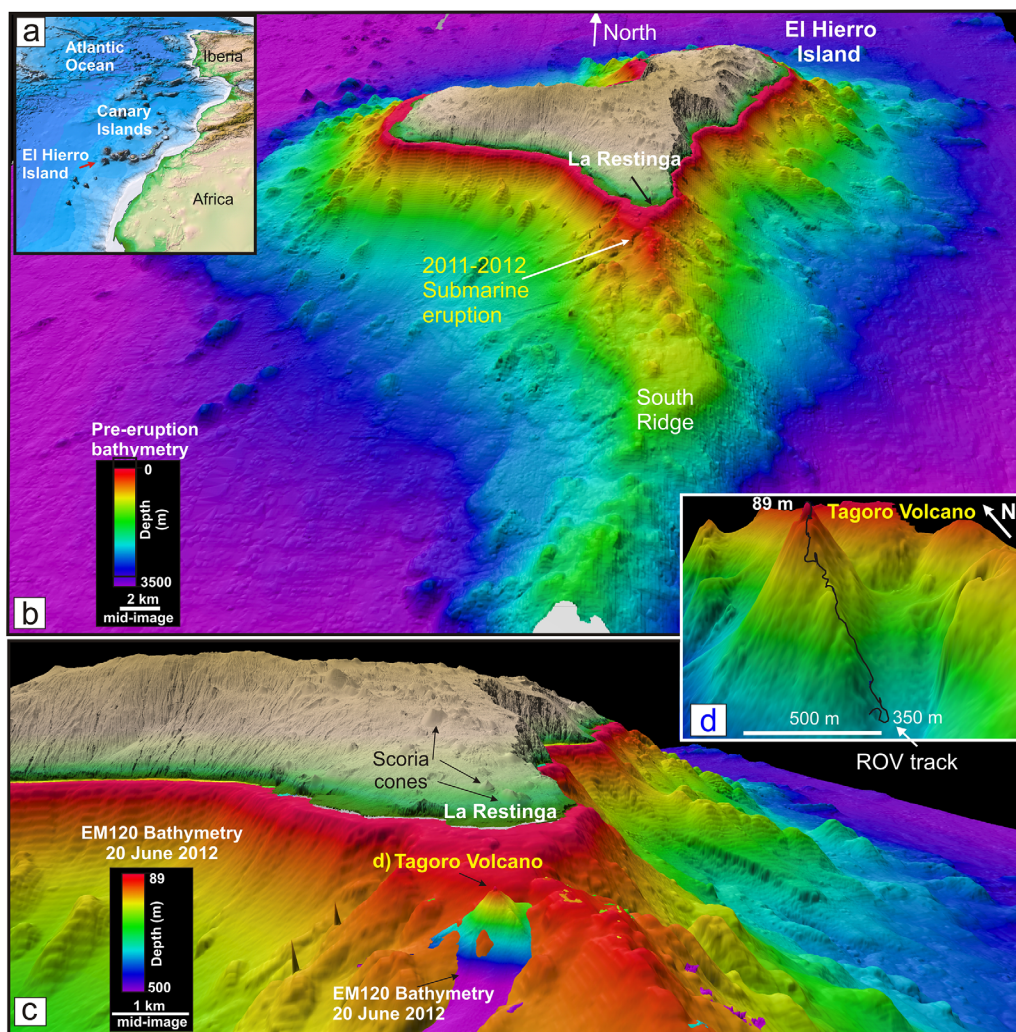
Figure 1. (a) Location of the Canary Islands; (b) 3-D digital terrain model of the El Hierro Island before the eruption, a triple-arm rifted oceanic island; white arrow show location of the 2011 submarine eruption on their south rift; (c) 3-D model of the multibeam bathymetry from 22 December 2011 superimposed to pre-eruption terrain model. Water depth scale for the submarine edifice on the left; (d) final morphology of the Tagoro volcano. Bathymetry from 28 June 2012. The ROV track is also shown.

is known about submarine eruptive processes as they are inherently difficult to observe or sample in detail, especially during explosive phases [*Arculus*, 2011; *Rotella et al.*, 2013]. Most interpretations of underwater eruptions have been based on post-eruptive deposits sampled by dredging the seafloor [e.g., *Somoza et al.*, 2004; *Barker et al.*, 2012; *Conte et al.*, 2014], through remotely operated vehicle (ROV) observations of volcanic features and direct sampling [e.g., *Binard et al.*, 1992; *Fouquet et al.*, 1998; *Stern et al.*, 2008; *Schipper et al.*, 2010a, 2010b, 2011; *Murtagh and White*, 2013] or from field studies of uplifted ancient deposits now exposed on land [e.g., *Allen and McPhie*, 2009]. Although these studies have provided extremely valuable insights into submarine eruption dynamics and generated a range of plausible eruptive models, they are restricted by a lack of context with respect to the eruptive sequence. For example, dredging or surficial sampling often only captures material from a single phase of an eruption or deposits may be reworked with multiple sources and lack stratigraphic context [e.g., *Barker et al.*, 2013]. Even if layering or eruptive stratigraphy is preserved, the very nature of eruptions into water means that not all material will be accurately represented in seafloor stratigraphy, as some material (e.g., fine grain size or highly vesicular pyroclasts) may float and be distally deposited [e.g., *Fiske et al.*,1998; *Allen et al.*, 2008; *Rotella et al.*, 2013; *Troll et al.*, 2012]. In contrast, studies of active eruptions [e.g., *Embley et al.*, 2006, 2014a, 2014b; *Soule et al.*, 2007; *Deardorff et al.*, 2011; *Rubin et al.*, 2012] are relatively rare due to the difficulty and cost of rapidly mobilizing recording and monitoring equipment to the isolated locations that submarine eruptions often occur in. One of the remaining challenges in submarine volcanism is, therefore, not

only documenting real-time eruptive processes, but also recording the growth and evolution of submarine vents throughout the eruptive sequence and then relating the observed processes and deposits back to eruptive styles and proposed conceptual models [e.g., *Head and Wilson*, 2003; *White et al.*, 2003].

In July 2011, frequent short-period earthquakes were detected by the Spanish Instituto Geográfico Nacional (IGN) beneath El Hierro, the westernmost and youngest island [*Guillou et al.*, 1996] of the Canary archipelago (Spain) (Figures 1a and 1b). More than 12,500 small earthquakes were detected over the preceding 3 months along with minor surface deformation and gas emissions [*López et al.*, 2012]. By the end of September, the location of seismicity migrated from an area north of the island to the south by 14 km, interpreted as signals produced by the magma rising from a deeper central source (9.5 $\pm$ 4.0 km), which correspond to the depth of the Moho (mantle-crust transition) and a shallower magma reservoir at the flank of the southern rift (4.5 $\pm$ 2.0 km) [e.g., *Becerril et al.*, 2013; *González et al.*, 2013; *Carracedo et al.*, 2015]. Very shallow earthquakes on 10 October 2011, continuous harmonic tremor, dead fish, and patches of pale colored water at the sea surface indicated the onset of a submarine eruption at about 300 m water depth and at ~5 km distance from the town of La Restinga [e.g., *Carracedo et al.*, 2012a; *Pérez-Torrado et al.*, 2012]. The El Hierro eruption formed a new submarine cone by the end of October (Figure 1c) and continued as monitored by seismic tremors through until late February when seismicity decreased drastically until 6 March 2012, when the red alert originally issued by IGN was removed. Since 2016, the new volcano appears on the official hydrographic charts as "*Tagoro*" (meaning "stone circle for meeting place" in the aboriginal Canaries language).

The 2011–2012 El Hierro event is extremely significant, being among the first submarine eruption worldwide to be fully monitored in real time since the beginning of unrest, similar to the long-term monitoring of the eruptions of the Axial Volcano in 1999 and 2011 [e.g., *Embley et al.*, 1999], NW Rota-1 volcano [*Embley et al.*, 2006], or West Mata Seamount, NE Lau Basin [*Embley et al.*, 2014a]. As such, there have been many publications documenting precursory activity [e.g., *López et al.*, 2012; *Pérez et al.*, 2014], the geophysical signatures of magma movement [e.g., *Ibáñez et al.*, 2012], the geochemical origins of the magmas [e.g., *Troll et al.*, 2012; *Martínez-Frías et al.*, 2012; *Martí et al.*, 2013a, 2013b; *Meletlidis et al.*, 2012; *Rodríguez-Losada et al.*, 2015] and the formation of the submarine edifice [e.g., *Somoza et al.*, 2012]. Here we combine real-time monitoring information and sea-surface observations with the results of several bathymetric surveys carried out before, during and after the 2011–2012 event to document the evolution and nature of the submarine eruption and the main features of the new Tagoro volcanic cone. We use hydroacoustic and ROV observations to interpret the different stages of the eruption and their associated vents, plume types and deposits, and compare these with proposed eruptive models for submarine volcanism.

2. Survey Summary and Methods

Multibeam mapping of the volcano morphology and hydroacoustic images of the submarine plumes were obtained in three legs: two during the GAIRE-2011 cruise onboard the R/V *Sarmiento de Gamboa* (28–29 November 2011 and 22 December 2011) and one during the AMULEY-2012 (20–28 June 2012) cruise onboard R/V *Hespérides* (supporting information Text S1). After the eruption, the survey SUBVENT-2 (4 April 2014) onboard the R/V *Sarmiento de Gamboa* allowed ROV inspection and direct sampling of the volcanic products sourced from the 2011–2012 undersea eruption. Multibeam bathymetry echo-sounder (MBES) data from R/V *Sarmiento de Gamboa* were acquired with an Atlas Hydrosweep Ds 1 $\times$ 1 deep-sea multibeam echosounder during the main process of volcanic eruption. SIPPICAN XBT depth-temperature measurements were made periodically with a precision of $\pm 0.15°$C for acoustic corrections of the water speed (supporting information Text S1). Post-eruption bathymetric data (22 and 28 June 2012) from R/V *Hespérides* were acquired with Konsberg EM120 deep-sea multibeam echosounder. Real-time surface sound-velocity corrections were conducted using a SVPlus V2 AML and XBT SIPPICAN MK-2 (eXpendable Bathy-Thermic Sounds) probes. Processed bathymetry was performed using the software Caris HYPS. Processed bathymetry grid cell size ranges between 15 and 20 m. To quantify the volumetric changes, we used ArcGIS tools to create 30 m grid cell size between the 22 December 2011 bathymetry grid (the only deep-water bathymetry survey carried out during the eruption) and the older data set before the eruption provided by the Spanish Navy Hydrographic Institute (IHM) (supporting information Figure S1 and Text S1).

The water column was acoustically surveyed using three types of echosounders at six different frequencies: parametric echosounder Atlas PARASOUND P-35, Konsberg EA 600 and EK 60. These echosounders yield a

volume backscattering coefficient in decibels (reflectivity). Two different frequencies were used with the parametric echosounder Atlas P-35: a Primary High Frequency (PHF) at 20 kHz and a Secondary Low Frequency (SLF) at 4.5 kHz. The water column was recorded with the PHF mode using a high cut filter of 6 kHz, whereas the subseabed was recorded using the SLF mode. The biological echosounder Konsberg EK 60 was also used simultaneously working at different frequencies (38 and 120 kHz) with the standard Konsberg EA 600 echosounder working at 12 and 200 kHz, providing outstanding images of the plumes during the main eruption stage (November and December 2011). The PHF mode of the parametric Atlas PARASOUND P-35 yielded very high-quality hydroacoustic images of the volcanic plumes. Processing of Konsberg echosounder data was performed using the Echoview software in order to transform data from time to real position. The PHF mode data of the parametric echosounder was transformed using Kingdom Suite software.

Submersible observations and sampling of the volcano were carried out during the SUBVENT-2 survey onboard the R/V *Sarmiento de Gamboa* using the ROV *Luso* (supporting information Text S1), run by the Estrutura de Missão para a Extensão da Plataforma Continental (EMEPC), equipped with a high definition camera (1024 × 1024 pixel digital still camera), two robotic manipulators for the recovery of biological/geological samples, CTD (conductivity, temperature, and depth measurement) with fluorescence, turbidity and CO_2, CH_4, and O_2 sensors, and 4 Niskin bottles for water samples. The track of the ROV was planned using previous multibeam mapping in order to cross the former 2011–2012 eruptive centers from ca. 380 m water depth to their summit located at ca. 89 m water depth (Figure 1d). More than 20 rock samples were recovered during the visual observation of the ROV from the deeper parts of the submarine cone at 347 m water depth to the summit at 90 m water depth (supporting information Table S1) following the track planned based on 20–28 June 2012 MBES model.

Analyses of nine representative rock samples recovered by ROV (supporting information Table S2) were carried out in the Central Labs of the Geological Survey of Spain (IGME). Polished thin sections of volcanic rocks were prepared and studied under the petrographic microscope to record textural and mineralogical features (supporting information Figures S5–S8). Whole-rock major and trace elements contents were analyzed by X-ray fluorescence (XRF) using a MagiX of PANalytical instrument with Rh radiation. Na_2O was measured using a VARIAN FS-220 atomic absorption spectrometer. Accuracy of the data was checked by using international standard reference materials, and precision based on duplicate samples was found to be better than ±5%. Loss on ignition (LOI) was determined by calcination at 950°C. Rare Earth Elements plus Yttrium (REY), Th and U concentrations of selected samples were determined by Inductively Coupled Plasma Mass Spectrometry (ICP-MS) using an Agilent 7500 CE instrument. The standard reference material MLB-1 (USGS) were used to test the analytical procedure for REY determinations. The accuracy and precision obtained were better than 10% for all REY.

Detailed information about geophysical data, Remoted Operated Vehicle (ROV), samples, mineralogical, and geochemical techniques can be found in supporting information (supporting information Text S1, Figures S1–S9, and Tables S1–S4).

3. Results

### 3.1. Morphological and Volumetric Changes of the New Volcano

The El Hierro eruption started on 10 October 2011, within a pre-existing submarine valley off the port of La Restinga at 250–350 m water depth (Figure 2a). Initial bathymetry data collected by *Rivera et al.* [2013] on 25 October 2011, identified a single cone around 205 m water depth. Our bathymetric data from 29 November 2011 show that this volcano had slopes ranging 20–35° and between October and November, its summit had progressively shifted in a northwest direction, developing four vents with respective summits at 220, 195, 180, and 165 m water depth (Figure 2b). A large portion of the valley had also been filled by eruptive material by this time, consisting of several lobes with slopes of 10–12° outflowing from the emission center (Figure 2b). By 2 December 2011, two vents developed into a double cone, almost infilling the lower part of the valley. Our 22 December bathymetry shows a drastic collapse of the main edifice with respect to the survey carried out in November (Figure 2c). Previous collapse events were reported between 25 and 29 October and again between 31 October and 13 November 2011 [*Rivera et al.*, 2013, 2014]. The December collapse event resulted in almost 25 m decrease of the principal cone (from 145 down to 170 m water depth) and the development
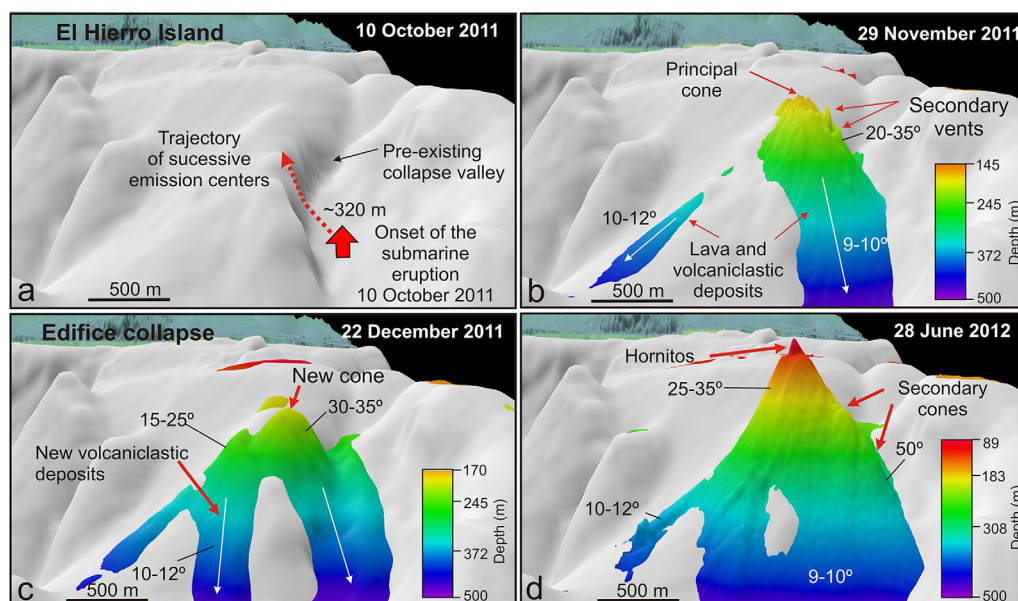
Figure 2. Fledermaus © 3-D images of the distinct multibeam bathymetric surveys showing the morphological changes of Tagoro volcanic edifice along the 2011–2012 submarine eruption: (a) the IHM98 pre-eruption model shows the pre-existing collapse valley; (b) the 29 November 2011 bathymetry shows several vents sourced from the main cone aligned along a southeast to northwest direction; (c) the 22 December 2012 bathymetry shows the collapse of the previous edifice forming a collapse caldera and the growth of a new cone; (d) the 28 June 2012 bathymetry shows the final morphology of the Tagoro volcanic edifice with the summit at 89 m water depth.

of a collapse rim, which is clearly identified in the bathymetry and the smoothing of previously steep slopes to 15–25° (Figure 2c). In addition, a new cone with slopes of 30–35° had grown inside the collapse structure, signaling the ongoing eruption. Eventually on the 24 February 2012 bathymetry, 137 days after the onset of the eruption, the shallowest summit of this new edifice was at 89 m water depth and a fissure eruption developed with at least four attached secondary cones following a north-northwest-south southeast lineation [*Vázquez et al.*, 2016]. The 22 and 28 June 2012 bathymetric data, acquired by our study, show the same morphology with the summit of the principal cone at the same water depth and the secondary cones along the southeast flank confirming that the main cone-building eruptive phase had ceased but degassing was still active (Figure 2d) [*Pérez et al.*, 2012]. The final morphology of the Tagoro edifice identified by our bathymetry on 28 June 2012 shows a principal cone with its summit at ca. 89 m water depth with flanks of 25–35° and secondary cones following an NW-SE trend along the southeastern flank.

The comparison between the pre-eruption bathymetric surveys and the bathymetry carried out after the collapse event 22 December 2011, highlights a series of positive depth changes assumed as volcanic accumulation from the onset of the eruption (Figure 3 and supporting information Figure S1). Based on this difference grid, we calculate 126×10^6 m^3 of nondense rock equivalent (NDRE) for the total volume of volcanic materials accumulated on the seabed after the collapse after 74 days of eruption. The comparison of bathymetry allow us to interpret the positive changes in the submarine topography as a result of volcanic deposition in the different morpho-depositional areas (Figure 3): on the summit (∼+112 m) and flanks (∼+35 m) of the submarine cone, on the proximal (∼+68 m) and distal (+35 to +55 m) deep-water volcaniclastic aprons and on scattered patches (+6 to +10 m) radially aligned from the eruptive center at runout distances between 1 and 10 km from the eruptive center. Based on these comparative maps, we have calculated the volume for the each of the main areas (supporting information Figure S1). The proximal area surrounding the eruptive vent (Figure 3b) composed by the volcanic cone and by a proximal volcaniclastic apron yields an accumulated volume of 39.1×10^6 NDRE m^3. The volcanic edifice comprising the cone, flanks, and the surrounding scoria block deposits yield an accumulated volume of 19.8×10^6 NDRE m^3 which corresponds to accumulation rates of 268×10^3 m^3 d^{-1} and 15% of the total material deposited. Downslope, the proximal apron (Figures 3c and 4) is 0.6 km × 1.2 m in size with average slopes of 9–10° and extend from 500 and 750 m water depth. Negative depth changes along the southern flank of the cone (−45 m) evidence large-scale landslides on the southern flanks sourcing this proximal volcaniclastic
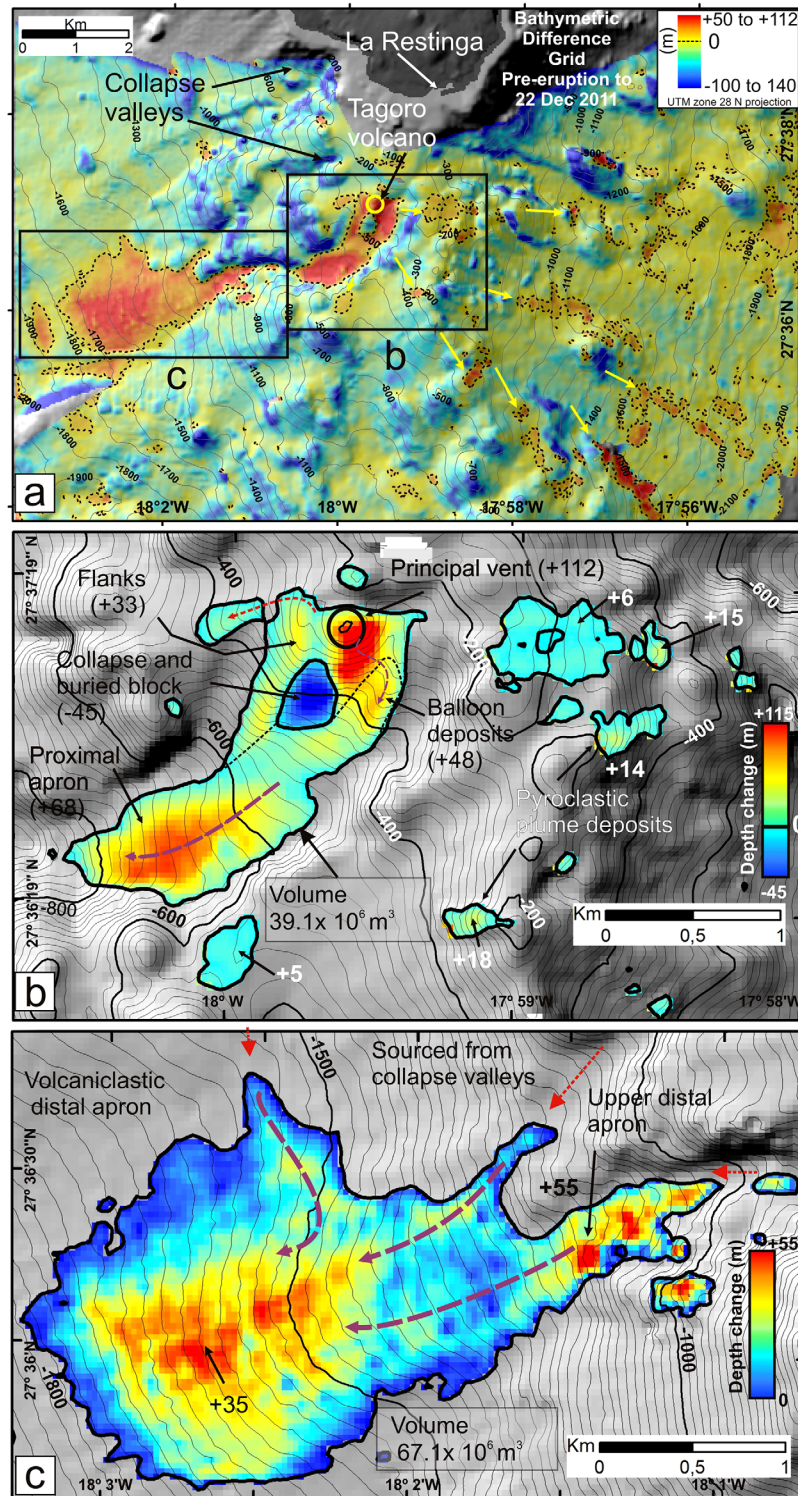
Figure 3. (a) Depth difference (rainbow color scale) grid depicting changes from the onset of the eruption (10 October 2011) to 22 December 2012 (74 days after) in a radius of ∼10 km around the eruptive center. The difference grid (see supporting information Figure S1) is overlain on pre-eruption bathymetric hillshade grid. Red colors correspond to maximum accumulation areas. Positive patches at the west of the emission center are interpreted as deposited from ash/lapilli buoyant plumes (yellow arrows). Blue colors are negative depth areas. Note collapse valleys surrounding the volcanic edifice. Bathymetry contours are every 100 m. (b) Accumulation areas in meters around the Tagoro submarine volcano: cone and flanks, lava balloons deposit, and proximal volcaniclastic apron. Note negative values reflecting large-scale landslide. (c) Accumulation in meters and total volume of the fan-shaped distal volcaniclastic apron. Note is sourced also from collapse valleys. Bathymetry contours are every 20 m.
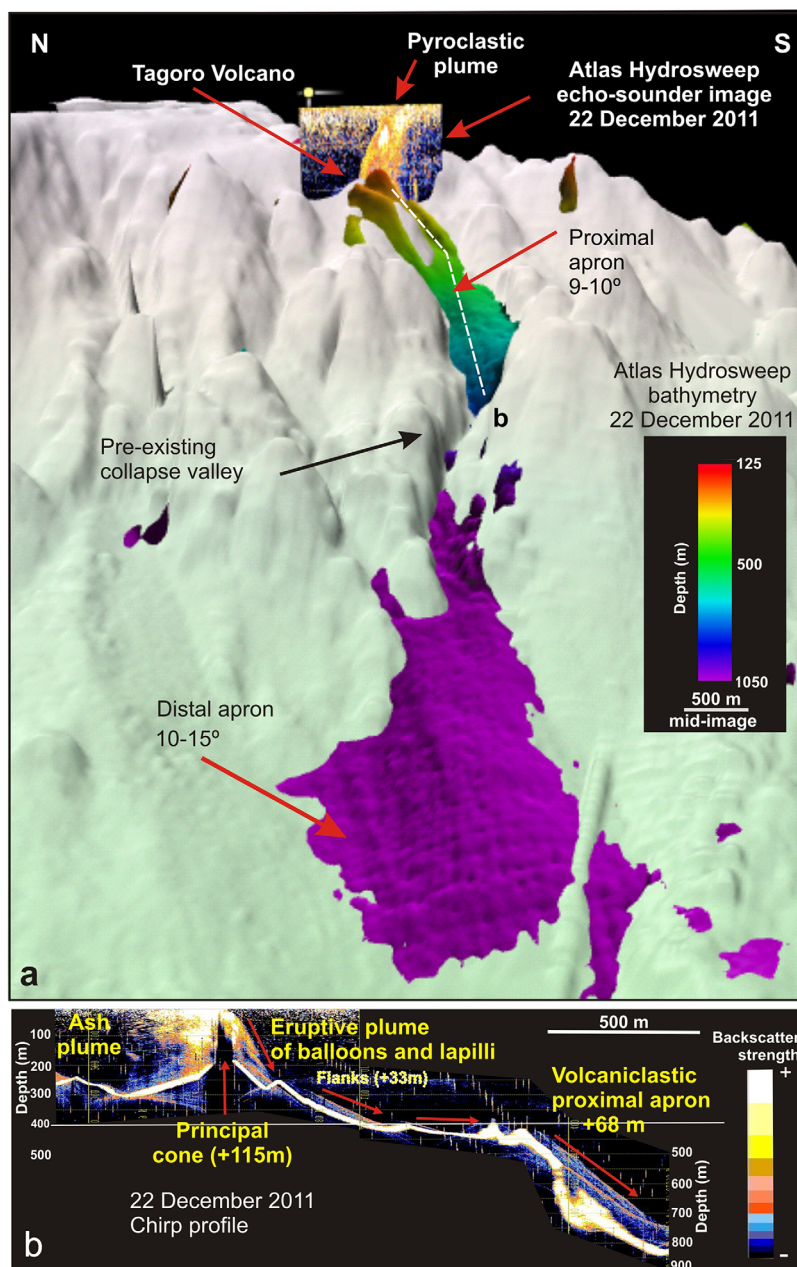
Figure 4. (a) Fledermaus © 3-D images made from a combination of the IHM98 pre-eruption bathymetry (white) and the 22 December 2011 bathymetry (color scale) during the eruption showing the proximal and distal volcaniclastic aprons developed after the collapse event. The image above the cone is the parasound high-frequency echo sounder showing the activity of the eruptive plume at this stage. (b) High-frequency parasound profile from the eruptive center to the proximal volcaniclastic apron composed by at least two collapse events. Note a near-bottom pyroclastic flow detached from the collapse of the main eruptive plume and flowing downslope. Location of profile is shown in Figure 4a.

apron. From the difference grid, we estimate that this proximal apron has a maximum thickness of 68 m and a total volume of ~19.3 × 10^6 NDRE m^3 at rates of 250 × 10^3 m^3 d^{-1} accumulated from the beginning of the eruption to the end of the collapse event (Figure 3c).

The volcanic deposits in distal areas are distributed into (i) a fan-shaped deep-water distal apron on the southwest side of the emission center and (ii) scattered patches of positive changes located the southeast principal cone (Figure 3a). A deep-water distal apron is clearly depicted by the difference grid (Figures 3c and 4). This apron is 3.2 km × 1.5 km in size with average slopes of 10–15°, and extends from 800 to

1080 m water depth. It is fan-shaped with thickness of 55 m at its upper part and 35 m at the lower part. The thickness pattern of this distal apron shows that is not only fed by the volcanic materials sourced from the eruptive center but also from the lateral collapse valleys (Figures 3a–3c). From the difference grid, we calculate a volume of $\sim$67.1 $\times$ 10^6 NDRE m^3 and average rates of 900 $\times$ 10^3 m^3 d^{-1} of erupted material deposited in this deep-water fan. We suggest that this high rate of accumulation, the highest in the volcanic system, is consequence of the collapse that occurred surrounding the volcanic edifice. In this way, large negative depth changes (up to $\sim$−140 m deeper on post-collapse survey) are located in the collapse valleys surrounding the volcanic cone (Figure 3b). Both volcaniclastic aprons, distal and proximal, accumulate a total volume of $\sim$86.5 $\times$ 10^6 NDRE m^3 which make up 68% of the total volcanic material deposited from the onset of the eruption to the end of the collapse events.

Scattered patches of positive depth changes (+6 to +10 m) aligned radially from the eruptive center are identified in the difference grid at the southeast side of the eruptive center (Figure 3a). The positive depth changes match with location and orientation of the dominant submarine plume transported by the prevailing undercurrents within the water column, as observed on aerial and high-resolution satellite images [e.g., *Eugenio et al.*, 2014]. We calculate a volume of 20.3 $\times$ 10^6 NDRE m^3 for the accumulation of volcanic material in theses distal areas deposited from the buoyant pyroclastic plumes in a radius of $\sim$10 km around the emission center (Figure 3a). These deposits make up 16% of the total volcanic material deposited on the seabed from the onset of the eruption to the end of the collapse event.

The distal deep-water apron (1000–1800 m water depth) and the patches deposited from the pyroclastic plume (200–2000 m water depth) were not included in the final eruptive volume calculated at around 329 $\times$ 10^6 NDRE m^3 by *Rivera et al*. [2013] because of the limitations of their multibeam echosounder (EM710)

below 1000 m water depth. Accounting for this extra volcaniclastic material for the distal deep-water apron ($\sim$67 $\times$ 10^6 NDRE m^3) and for the deposited from the suspended ash plumes ($\sim$20 $\times$ 10^6 NDRE m^3) we suggest a higher total eruptive volume of at least $\sim$416 $\times$ 10^6 NDRE m^3 or $\sim$0.4 km^3 of pyroclastic material.

3.2. Hydroacoustic Observations of Submarine Plumes and Their Temporal Variability

During our first survey at the eruption center on 29 November 2011, a large area of upwelling discolored seawater and floating pyroclasts marked the eruptive center (Figure 5a). Intense hydroacoustic plumes were recorded above the main cone during this time (Figure 6). The EK 60 echograms showed a dense curved rising plume with a high backscattering strength of up to −30 dB, sourced from the volcano summit and falling at 10–15 m below sea level (Figure 6a). The helicopter images taken during the GAIRE hydroacoustic survey on 29 November 2011, showed a huge milky green plume at the sea surface (Figures 5a and 5b) which correlates with the hydroacoustic images obtained by the single beam 38 kHz EK 60 and
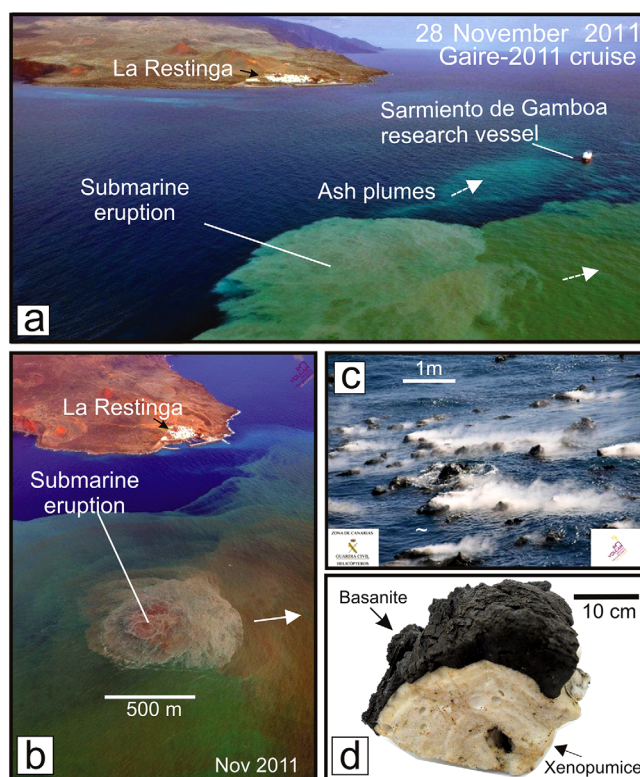
Figure 5. (a) Location of the oceanographic vessel *Sarmiento de Gamboa* surveying the active volcanic plume during the 28 November 2011 cruise. (b) Burst of gas and pyroclasts on the ocean surface off the nearby village of La Restinga (November 2011). (c) Steamed floating lava balloons at sea surface just before sinking (November 2011). (d) Xeno-pumices ejected by the eruptive plume and floating on the sea surface during the first days of the eruption (late October 2011). Aerial photos have been taken by the scientific flight INVOLCAN of the Civil Guard helicopter.
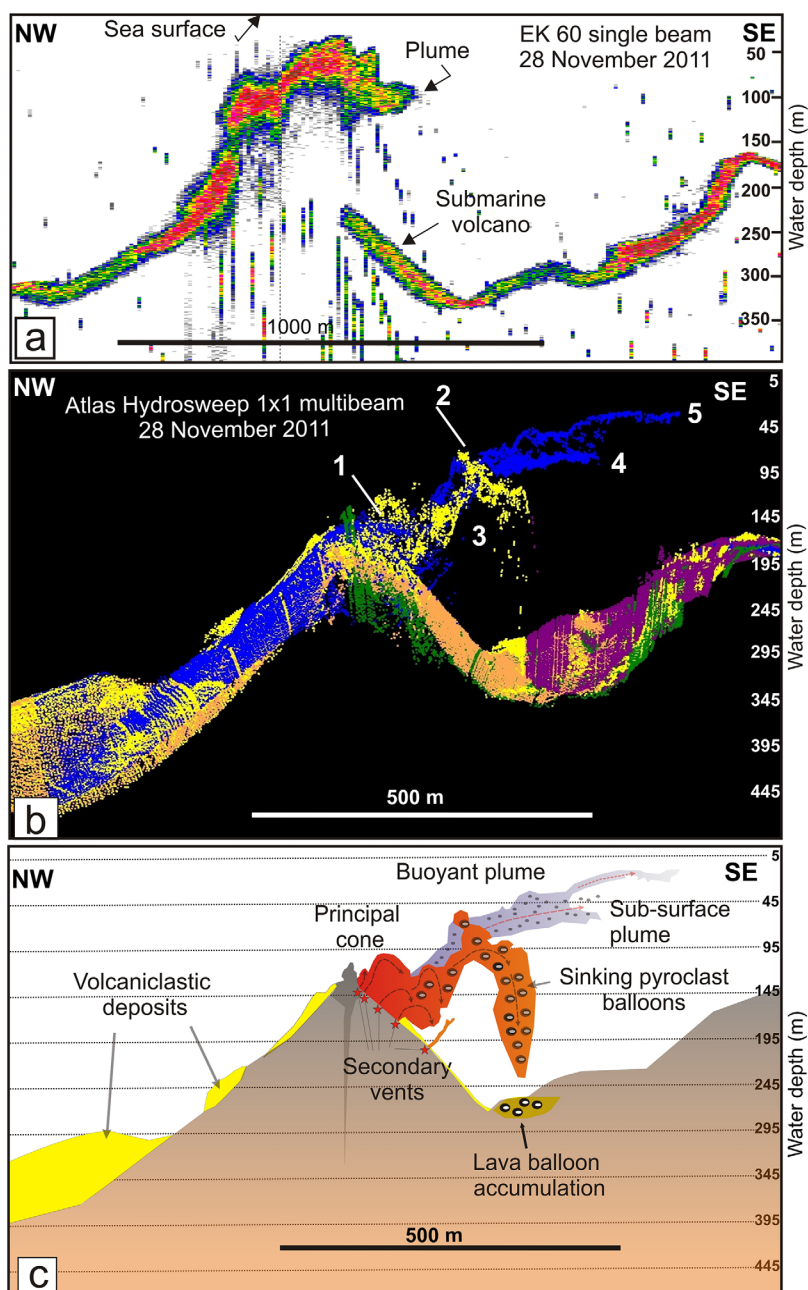
Figure 6. Hydroacoustic images of the subaqueous volcanic plume during the first phase of the eruption obtained the 28 November 2011: (a) Konsberg EK 60 (38 kHz) echo sounder; (b) Atlas Hydrosweep 1 × 1 (15.5 kHz) multibeam pings; and (c) their interpretation. Several buoyant high-backscatter volcanic plumes detached from the source vents can be observed on these acoustic images: two subsurface ash floating plumes (see also sea surface plumes along vessel track in Figure 5a) and a rain of pyroclasts and lava balloons.

multibeam 12 kHz Atlas Hydrosweep echo sounders (Figure 6). During this week, numerous steamed lava bombs appeared floating on the surface (Figures 5c and 5d) that after a few minutes began to sink. These surface observations are consistent with the image of the multibeam echo sounder pings that showed a neat plume floating on the water column (Figures 5b and 5c). The submarine plume is comprised first by a dense segment sourced from the four emission vents located along the slope of the main cone at 220, 195, 180, and 165 m water depth (1 in Figure 6b). This dense segment appears to gradually shallow to reach 20–30 m below sea surface and then, collapse and continue down toward the seafloor (2 in Figure 6b). Scattered spots detached and falling from the bended plume (3 in Figure 6b) are interpreted as the sinking of lava balloons observed floating on the sea surface. The large steaming pyroclasts observed at the surface
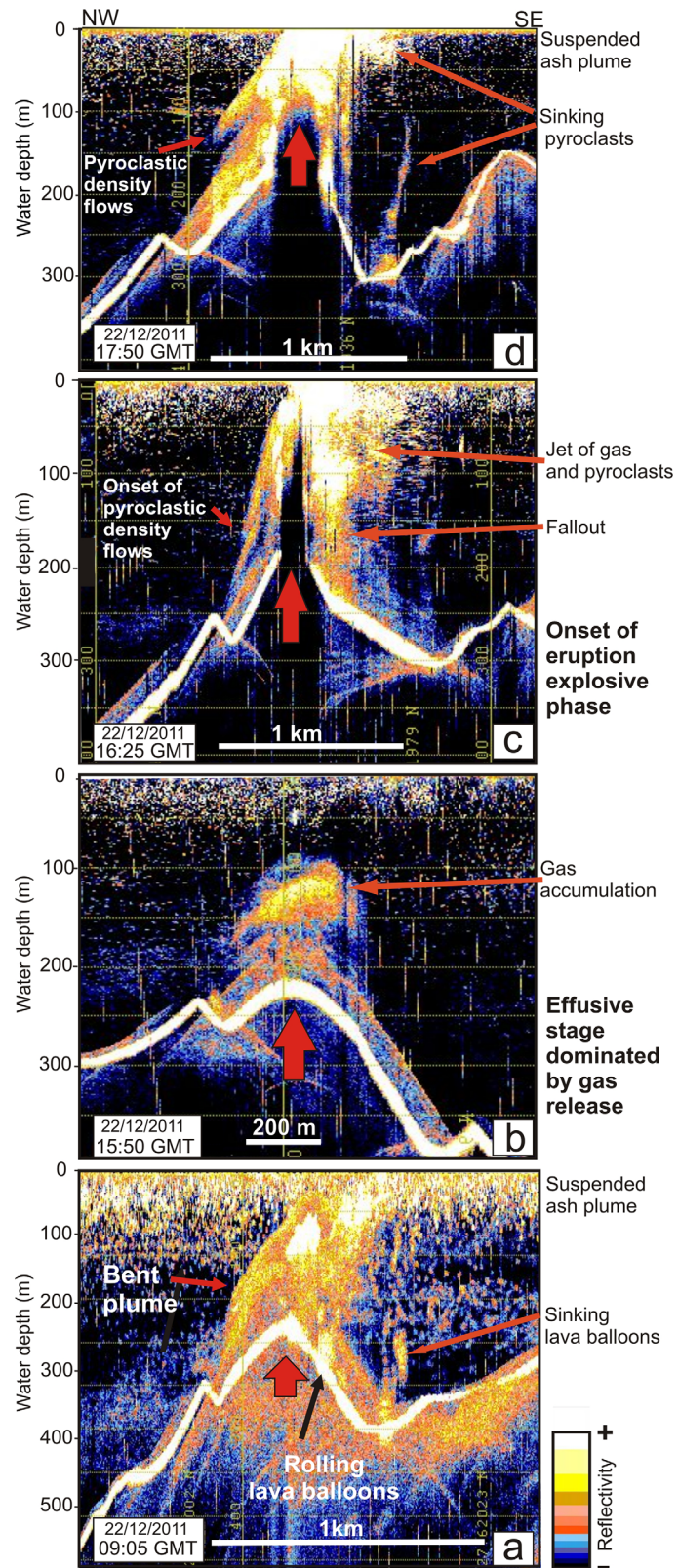
Figure 7. (continued)

were buoyant when initially erupted and then quickly began to sink when they crossed over buoyant to nonbuoyant (Figure 5c). The hydroacoustic image from 28 November suggests that high-reflectivity spots did not reach the sea surface, descending to the seabed but not above the emission centers (Figures 6b and 6c). Another branch of the main erupted plume was split up into two horizontal entrainment plumes. The lower one extended horizontally at 20 m depth below sea surface (4 in Figure 6b), whereas the upper one rose gradually toward the surface (5 in Figure 6b). Both of these parts of the dominant submarine plume coincide with finer grain-size buoyant lapilli and fine suspended ash (supporting information Figures S4 and S6) that are transported by the prevailing undercurrents within the water column, as observed on aerial and satellite images (Figure 5, supporting information Figures S2 and S3). The plume at this time was up to 30 km wide and 100 km along the south part of El Hierro Island [*Eugenio et al.*, 2014].

The 22 December 2011 hydroacoustic images taken after the collapse of the first edifice contrast significantly from those previously observed (Figure 7). Here the bathymetric profile not only shows lower bathymetry values than that of 29 November 2011 (Figure 2b) but it also presents a possible scarp of the cited flank collapse (Figure 2c). The sequence of four images of the hydroacoustic plumes obtained at intervals of one and half hours with the PHF mode of the parasound allow us to observe significant temporal changes in terms of the dynamics of the eruption and resulting submarine eruptive column (Figures 7a–7d). A range of hydroacoustic plume types was identified over this time sequence. The first image at 09:05 GMT showed a curved, low intensity plume that lacks a high-backscatter region above the main cone but contains at least two bright spots of high backscatter values toward the upper part of the rising material which spans the entire water column (Figure 7a). Also in a similar fashion to the November plume (Figure 6), the December plume is curved toward the sea surface and fallout of steam-charged bombs is observed in the water column on the flanks of the volcano (Figure 7a). After a 6 h interval (15:50 GMT), this plume appeared totally disconnected with the sea surface, restricted to >100 m water depth and centered over the main cone. Given the flat shape of the plume it is likely reflecting gas accumulation from the release of exsolved volatiles from magma during a hiatus in activity or an effusive phase of the eruption (Figure 7b). After less than an hour (16:25 GMT), the eruption increased significantly in energy. A large eruptive jet-like structure spanning the entire water column was observed and is interpreted as an explosive phase of the eruption (Figure 7c). The base of this plume is represented by a high-backscatter region forming a vertical eruptive column, with material spreading and then falling vertically from the plume and flowing downslope along the flanks of the edifice. The last image taken one and a half hours after (17:50 GMT) shows a sustained plume with a similar morphology to that previously observed at 9:00 GMT but with a thicker base to the plume and backscatter signals on the flanks of the volcano representing the development of large submarine density currents down the NW slope and sinking of ash and pyroclasts forming a superficial plume on the SE slope (Figure 7d). Sea-surface activity during this time showed periodic events of increased bubbling and suspended volcaniclastic material on the sea surface with values of pH around 5.

3.3. Remotely Operated Vehicle (ROV) Observations

Several types of deposits were imaged and sampled by the ROV *Luso* after the eruption had ceased that can be directly compared with the changing cone morphology as documented by multibeam bathymetric mapping and hydroacoustic images. The ROV track was planned with our bathymetry from June 2012 from the base to the summit of the Tagoro edifice rising along the southeast flank in order to observe and sample the multiple types of eruptive deposits (Figure 1d and supporting information Figure S4). In this way, we suggest that the majority of the ROV observations are of deposits formed after the major collapse of the initial edifice in December. We have divided the final deposits observed by ROV around the new Tagoro edifice into four distinct geomorphic zones, each of which provides evidence for a range of eruptive styles.

Figure 7. Sequence of hydroacustic images obtained during the second phase of the eruption of the Tagoro volcano. These images were obtained by continuous surveying above the active submarine eruption volcano from 9:05 to 17:50 GMT (22 December 2011) using the Primary High Frequency (PHF) mode of the ATLAS parasound echo sounder (20 kHz). These images show a sequence of effusive to explosive eruptions. From bottom to top: (a) a weak plume reaches the sea surface and generates a rain of steamed lava balloons; (b) an effusive stage with accumulation of gasses after almost six hours; (c) the explosive plume reaches the sea surface and begins to expand laterally; (d) a stream of ash and lapilli pyroclasts appear sinking detached from the bursting plume. In addition, secondary plumes interpreted as pyroclastic flows are also detached from the burst flowing along the flanks of the cone (see Figure 4).
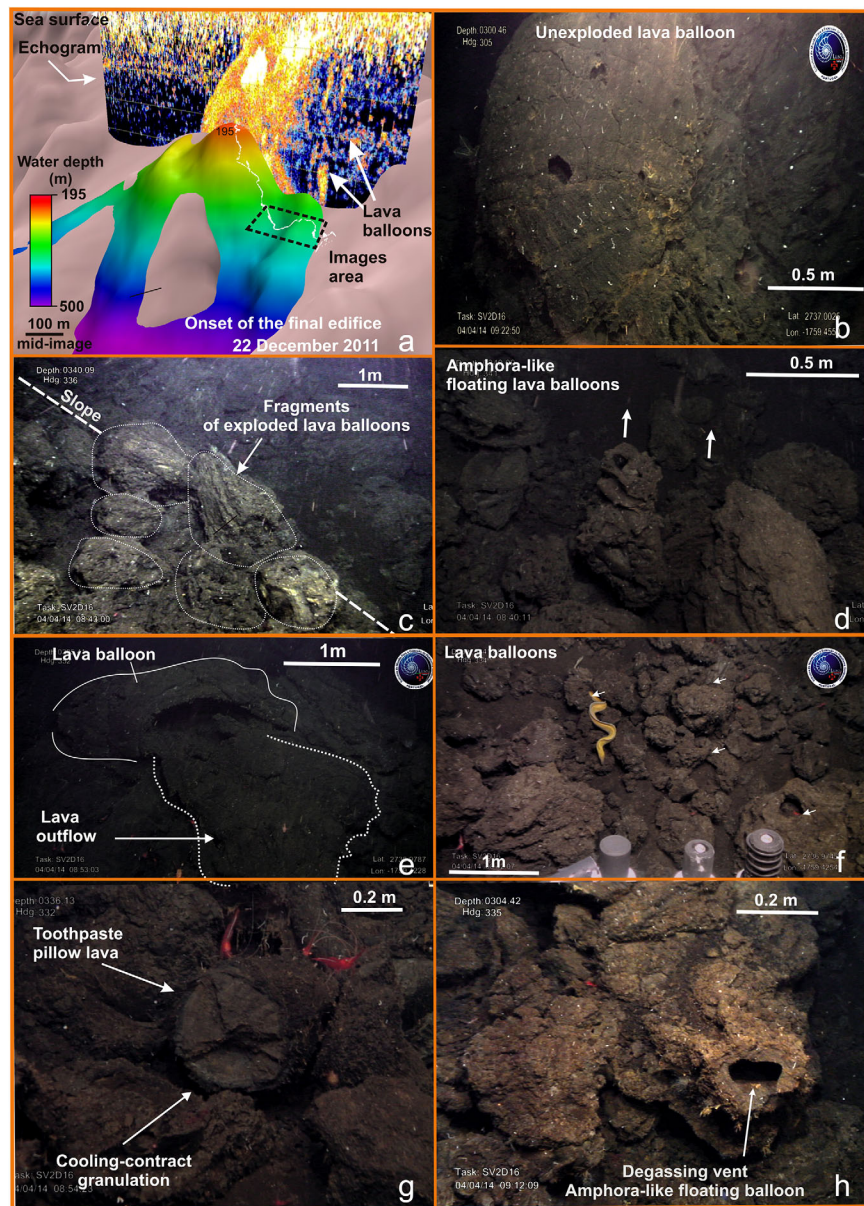
Figure 8. Submersible images depicting the types of giant scoriaceous lava products located at 300–350 water depths; (a) location of the area (dashed square) where the submersible images were taken referenced to the bathymetry and echo sounder image from the 22 December 2011. The ROV track is also shown. This echo sounder image shows high-backscatter bright spots interpreted as lava balloons falling down and deposited in this area. (b) Giant lava balloon with degassing orifices (300 m water depth). (c) Accumulation of fragments of lava balloons along steep slopes (340 m water depth). (d) Fragment of a lava balloon resembling a rift-type breaching showing a well-developed external crust (298 m water depth). (e) Mega balloon showing spreading out of lava flow over the sea floor (305 m water depth). (f) Vertical amphora-like floating lava balloons showing degassing orifices (340 m water depth). (g) Degassing vent observed on a lava amphora-type floating balloons (335 m water depth). (h) Accumulation of ellipsoidal floating lava balloons (334 m water depth).

3.3.1. Base of the Tagoro Edifice: Lava Balloon Accumulations

The base of Tagoro edifice is dominated by an area with extensive accumulations of scoriaceous bombs at water depth ranging from 280 to 380 m (Figures 8b–8h). When observed closely with the ROV these bombs appear to be either whole intact lava balloons or broken fragments of larger balloons. We have identified three dominant types of lava balloons that occur from the most proximal to the most distal areas: (i) giant lava balloons >1 m in diameter (Figures 8b, 8c, and 9b), (ii) amphora-like balloons (Figures 8d and 8h) and (iii) ellipsoidal balloons (<1 m in diameter) and fragments of exploded lava balloons (Figure 8f).
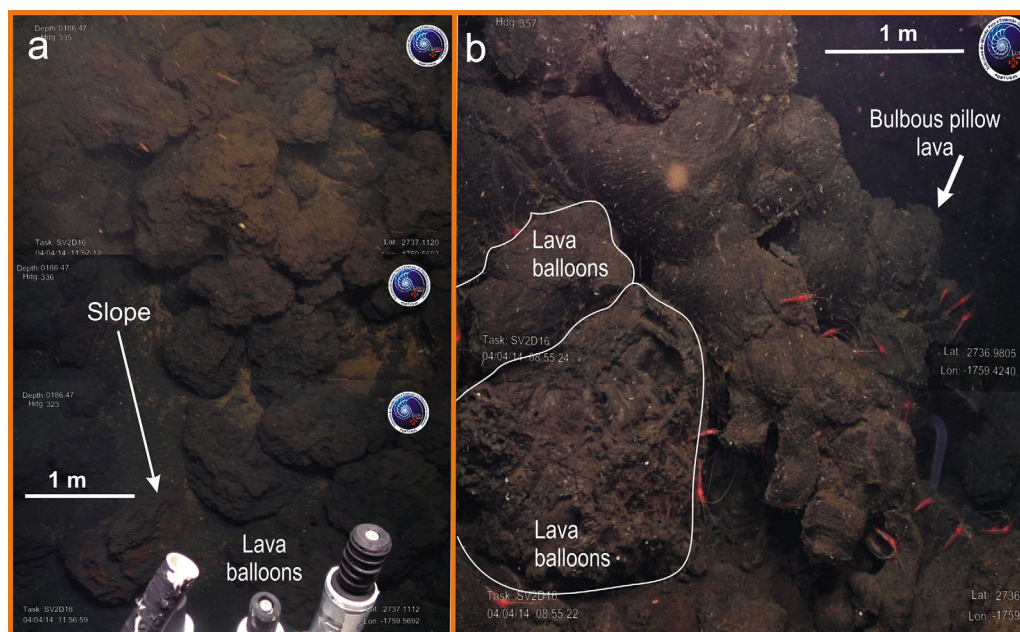
Figure 9. Images of giant vesicular lava balloons and lava stalactite pillows; (a) massive accumulations of lava blocks forming >45° steep slopes (335 m water depth); blocks are >1 m; (b) bulbous pillows forming lava stalactites by flowing downslope over the massive accumulation of lava blocks (357 m water depth).

The giant lava balloons (Figure 8b) are deposited along the most proximal segment of the slope at 280–340 m water depth (Figure 9a) and are characterized by average diameters of ≥2 m, but reaching up to more than 4 m. Their external surface is glassy showing contractional cracks and bread-crusted quenched surfaces (Figure 8b). Some lava balloons show evidence for lava spreading from their center at the seafloor, indicating that lava remained hot enough to flow plastically over the seafloor after breaking out from the balloon crust post-emplacement (Figure 8e). Some of the largest examples show large voids occur within the cores of the balloons (Figure 9b). Unexploded lava balloons form large stacks with maximum slopes of 45° along the lower flank of the Tagoro volcano, in some cases, overlaid by bulbous pillow lavas from the secondary fissure vents (Figure 9b). Hydroacoustic images obtained in December 2011 showed distinct acoustic spots in the water column, not reaching the sea surface, sinking toward the seafloor after being ejected from the principal cone (Figure 7a). The location of these acoustic spots coincides with the accumulation of giant lava balloons on the seafloor as observed by ROV, confirming our initial interpretations.

The second type of deposits found in the deeper, more distal parts of the volcanic cone slopes are the "amphora"-like balloons (Figures 8d and 8h) which have been named after their shape resembling a "roman amphora" with an open orifice at its top. The aerial photographs taken during the most active period of eruption showed how massive floating balloons often appeared on the surface with active degasification vents on their top (supporting information Figures S2 and S3). Once sufficient degassing and cooling had taken place, the floating balloons began to sink rapidly. The amphora shape may be related to vertical molding of hot plastic lavas sustained by the upper degassing vent at the sea surface. This type of amphora-like balloons shows large degasification conduits directed upward to the top of the balloon (Figures 8d and 8h) indicating that they sank vertically keeping the degasification conduit in an upright position. In many cases, amphora balloons are deposited on the seafloor with their degassing pipes still facing in a vertical direction, highlighting their relative buoyancy in water (Figure 8d).

The third and most distal types of deposits are formed by ellipsoidal lava balloons with less than 1 m average size (Figure 8f). They occur as large accumulations at the foot of the cone between 300 and 350 m water depth. Ellipsoidal balloons are much more oval than the "amphora"-like balloons and smaller than the giant lava balloons and their wider distribution likely reflect rapid quenching and preservation due to
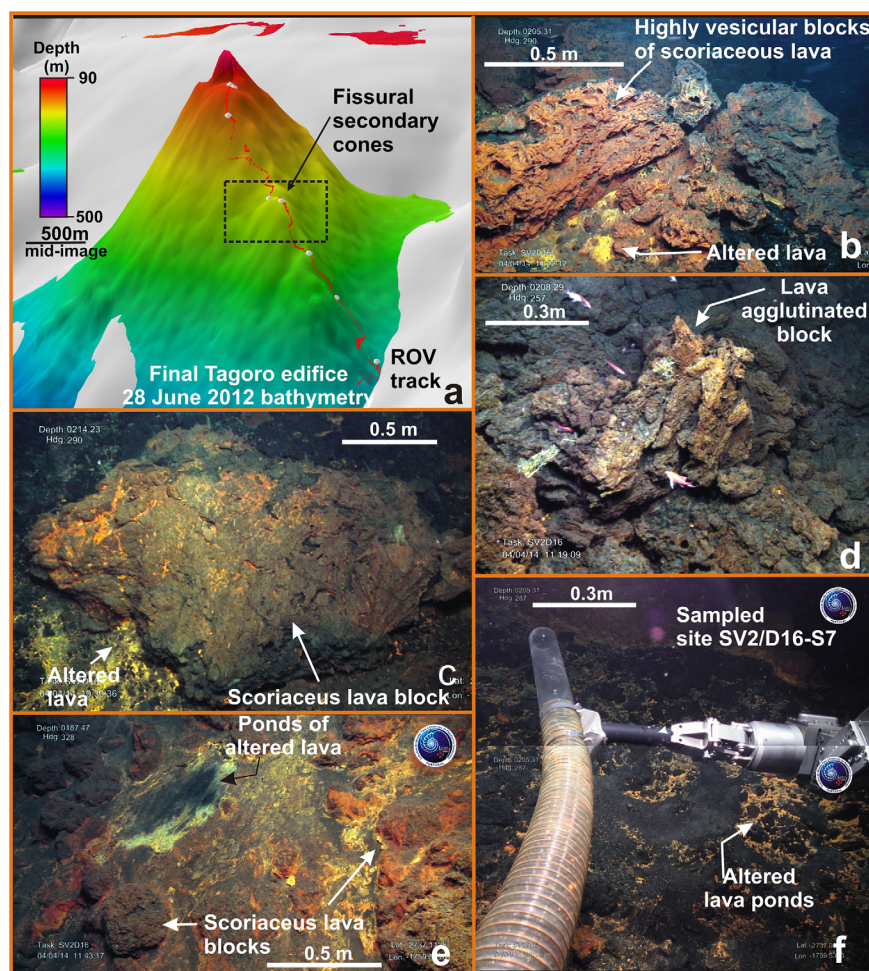
Figure 10. ROV images of the secondary cones along the SE flank of the Tagor volcano: (a) multibeam bathymetry image from the 26 November 2011 where several secondary cones can be identified at water depths between 195 and 165 m. (b) Scoriaceous brownish welded lava blocks with large vesicles (205 m water depth). (c) Block of scoriaceous lava overlying a zone of hydrothermal yellow alteration (214 m water depth). (d) Agglutinated and welded scoriaceous breccia (208 m water depth). (e) Ponds of highly hydrothermal altered flat seafloor (black and yellow) surrounded by scattered scoriaceous lava blocks interpreted as an active vent (187 m water depth). (f) Flat surface with altered deposits (brownish) mixed with lapilli deposits (black) (205 m water depth). This lava pond interpreted as an active vent is rimmed by agglutinated brownish scoriaceous lavas.

their size. They do not show any evidence for degassing pipes or large internal void spaces. Numerous floating balloons matching these deposits appeared at sea surface during the two stages of the eruption (Figure 5c). Many floating and steaming balloons observed at the surface during this time only stayed afloat for a few minutes before slowly sinking (supporting information Figures S2 and S3).

3.3.2. Secondary Fissure Vents: Effusive Scoriaceous Lava and Hydrothermally Altered Lava Ponds

At least four secondary cones were developed in the last stage of the eruption along the southeast flank of the edifice, along a SE-NW fissure structure (Figure 10a). Our ROV track crossed at least two of these secondary vents at water depths between 220 and 205 m (Figure 10a). These vents are characterized by flat surfaces of strongly altered lavas and scattered blocks of scoriaceous breccia that grade laterally to agglutinated blocks of brownish scoriaceous lava (Figures 10b–10f). The hydrothermally altered lavas are represented by multicolor (white, black, and red) seafloor patches and the scoriaceous lava is composed of large (~1 m) brownish heterometric and subangular blocks showing coarse vesicular textures and degassing conduits (Figure 10d). The lavas are then draped by a thin layer of dark grey ash that was also sampled for analysis (Figure 10f, SV2/D16-S7). Pillow lavas are observed in the most distal deposits as flowing over the accumulation of lava balloons on the lower slopes of the secondary vents (Figure 9b), indicating that effusive activity from these vents preceded the earlier ejection of lava balloons.
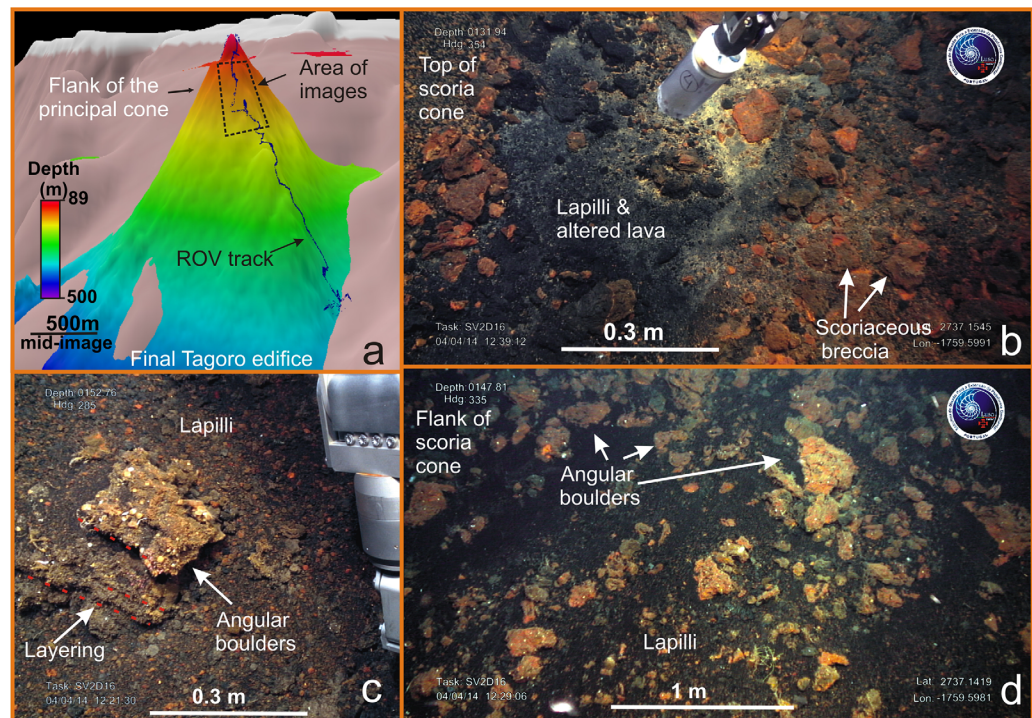
Figure 11. ROV images of the deposits along the flank of the principal cone between 180 and 120 m water depth: (a) area of the ROV images showed on the bathymetry from June 2012; (b) altered hydrothermal surface (white) surrounded by a breccia of scoriaceous lava (131 m water depth); (c) detailed of an ejected angular boulder overlying massive lapilli deposits on the flank of the principal cone (152 m water depth); (d) Lapilli and finer ash deposits alternating with highly heterometric brownish angular boulders forming the 25–35° flanks of the principal cone (147 m water depth).

3.3.3. Flanks of the Principal Cone: Accumulation of Ejected Angular Boulders

Extensive pyroclastic deposits cover the slope of the principal cone of the Tagoro edifice at depths between 180 and 115 m (Figure 11a). These deposits consist of a range of grain sizes including lapilli and finer ash deposits alternating with highly heterometric brownish angular boulders (Figures 11b–11d) with an overall gradual increase in grain size (i.e., reverse gradation) upward. Some fragments preserved slight layering (Figure 11c) indicating that they might have been ejected as lithics from previous edifices formed at the summit through explosive eruptions. The largest heterometric lithics are intercalated between thinner layers of lapilli (Figure 11d). Upslope, massive scoriaceous breccia alternating with white seafloor patches of altered lava were identified on the ROV images being covered with fresh dark grey lapilli (Figure 11b).

3.3.4. Summit of the Principal Cone: "Hornitos" Lavas

A small upper cone developed on the principal cone in the final effusive stages of the eruption at the summit of the volcano at depths between 120 and 89 m (Figure 12a). This cone is characterized by the growth of 5 m high, conical to cylindrical structures composed of agglutinated pyroclastic products (Figure 12b). We refer to these features as "hornitos" which is the Canaries traditional name for the subaerial openings formed above the roof of lava flows. Hornitos are very common onshore volcanic structures in the Canary Islands and other areas such as Iceland [*Thordarson and Hoskuldsson*, 2002] or Hawaii [*Jurado-Chichay et al.*, 1996]. They are inferred to be formed during quenching of fluid lava, drawn up and spattered by magmatic gases or by heated trapped seawater. There are numerous hornitos at the summit of the submarine volcano, but they can be grouped in two morphological types as surveyed by the ROV. The deepest hornitos, located at ∼118 m water depth, are comprised by >5 m high, steep, and unstable walls, that stand out clearly on the morphology of the summit (Figure 11b). These hornitos show numerous degassing conduits punctuating their walls and marked by yellow mats, which are probably linked to sulfur-related bacterial activity (Figure 12c). The shallowest types of hornitos, located between 115 and 89 m water depth, are 4–5 m high, pyramid-like cones composed of agglutinated heterometric lava blocks (Figure 12d) with white potentially bacterial mats associated with the uppermost lavas (Figure 12e). Both
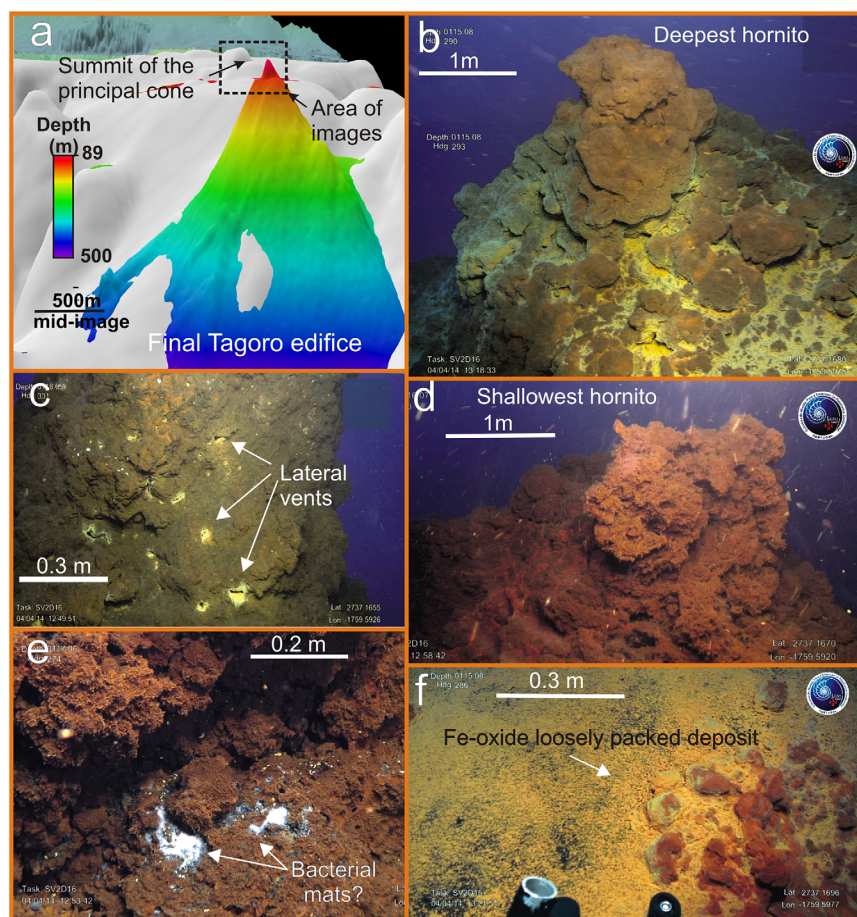
Figure 12. ROV images of the hornitos at the summit of the Tagoro volcano: (a) Location on the images on the multibeam bathymetry from the 28 June 2012. (b) Deepest hornito formed by 4–5 m tall pyramid-like of agglutinated lava blocks intermixed with yellow hydrothermal deposits (115 m water depth). (c) Detail of degassing vents (yellow orifices) along the flanks of the chimney interpreted as active hydrothermal vents (118 m water depth). (d) Top of the shallowest "hornito" (89 m water depth) showing abundance of red flocculates covering the lava deposits. (e) Detail of the flank of a hornito showing white bacterial mats. (f) Detail the tapestry of red to orange amorphous Fe-oxyhydroxide flocculates covering the overall summit of the Tagoro volcanic edifice.

the hornitos and the whole summit are covered by orange-brown, loosely packed Fe-oxides rich sediment that drapes the surface, potentially of microbial origin (Figure 12f and supporting information Figure S4).

3.4. Characterization of Volcanic Products

Previous studies of the products of the 2011–2012 El Hierro eruption have focused on material only collected from the sea surface [e.g., *Troll et al.*, 2012; *Martí et al.*, 2013a; *Longpré et al.*, 2014]. Here we use geochemistry to help constrain the origins of material collected in situ from the seafloor by ROV and also describe their textural features to help interpret the range of eruptive styles. The volcanic rocks recovered by ROV have been grouped according to the geomorphic zone where they were collected (Figure 12, supporting information Figure S4 and Table S1): (i) the deep floated balloon fallout area (347–268 m water depth); (ii) lapilli, ash, and scoriaceous lava from the secondary cones (220–205 m water depth); (iii) scoriaceous boulders from the flanks of the principal cone (154 m water depth); and (iv) hornitos lava at the summit of principal cone (115–89 m water depth).

3.4.1. Geochemistry and Mineralogy

All samples recovered by ROV (Figure 14) have broadly similar geochemical and mineralogical characteristics (supporting information Tables S2 and S3). They are classified as basanites based on the total alkalis-silica diagram of *Le Maitre et al.* [1989] (supporting information Figure S9), which is the most abundant and typical magma type of the Canary Islands and the dominant one in the rifts formed from the recent activity

of El Hierro Island [*Pellicer*, 1977; *Carracedo et al.*, 2001]. The ROV samples show low silica (41.2–41.9 wt %) and relatively high MgO (7.5–8.0 wt %), together with Ni (120–175 ppm) and Co (46–55 ppm) contents inside the range for primitive magmas (Ni: 90–670 ppm; Co: 27–80 ppm) [*Frey et al.*, 1978]. Compared to the *Martí et al*. [2013a] whole rock samples, our data show more restricted compositions. Major element variation diagrams (Figure 14) show that samples from *Martí et al*. [2013a] collected as floating pieces of lava balloons during the first stage of the eruption (October–December 2011) contain higher SiO_2 and lower MgO than our ROV samples with MgO contents progressively increasing from 5.56 to 7.8 wt % in those months (Figure 14a). On the other hand, samples published by *Martí et al*. [2013a] later in January are both slightly richer in SiO_2 and in MgO than our samples, and show some scattering in Na_2O and K_2O (Figure 14 and supporting information Table S2). Trace element concentrations of the seabed samples taken with the ROV also differ marginally from those collected floating on the sea surface in January, which have notably lower Nb and higher Zr concentrations than our ROV samples (Figure 14d).

Mineral compositions from seabed samples of the Tagoro cone (supporting information Table S4) are also more restricted and show less disequilibrium features than those described for the floating samples by *Martí et al*. [2013a]. Olivine phenocrysts and microphenocrysts are almost always normally zoned (Fo_{84} to Fo_{81} and Fo_{82} to Fo_{81} from core to rim, respectively), whereas olivine in the groundmass is Fo_{81}. Clinopyroxene (diopside) always show sector zoning, with #Mg ranging from 81 to 75. Oxide mineral inclusions in olivine phenocrysts and microphenocrysts contain chromium (3.5–8.5 wt % Cr_2O_3), whereas groundmass oxide minerals are titanium-rich (21 wt % TiO_2) magnetite with high MgO contents (>7 wt %). Plagioclase in the Tagoro samples is only present in the groundmass, and shows labradorite composition (An_{60-65}). All of these data fit mineral compositions described by *Longpré et al*. [2014] as belonging to the most primitive magma (magma 1) involved in La Restinga eruption. These compositions include: Fo_{88-82} olivines, 82–75 #Mg values for clinopyroxene and the occurrence of chromium rich oxide inclusions in olivine.

3.4.2. Textural Characteristics

All samples collected by ROV are porphyritic, with 5–20 vol % olivine and/or clinopyroxene phenocrysts and 35–75 vol % groundmass (supporting information Table S3). The groundmass can be either cryptocrystalline with microlites of olivine, clinopyroxene, opaque minerals, and needle-like plagioclase or glassy tachylite-sideromelane (supporting information Figures S5–S8). Despite their similar bulk chemical compositions, these samples display a range of textures and vesicularities, indicative of variable eruptive styles and degassing histories.

3.4.2.1. Lava Balloons

Floated lava balloon fragments (samples SV2/D16-R1 to R4, supporting information Tables S1 and S2) sampled from the lower cone flanks contain 40–50 vol % groundmass that ranges within individual samples from glassy in the clast rims to crystalline in the cores (Figure 13a and supporting information Figure S5). Bulk vesicularity of the lava balloon fragments are ~50 vol %, however, vesicularity as measured in thin section images varies significantly from rim to core, being ~60 vol % in the rim and <40 vol % in the core. Vesicle shapes and sizes also change sharply from rim to core, being spherical and typically <0.3 mm diameter in the rim and more irregular in shape and typically >1 mm in size toward the sample cores. Bubble shapes toward the clast interiors are indicative of coalescence and some vesicles are elongated in the direction parallel to the outer edge of the lava balloon (Figure 13a and supporting information Figure S5).

3.4.2.2. Lapilli and Ash From the Secondary Fissure Vents

Moderately to highly vesicular lapilli and glassy ash-sized particles were recovered above altered scoriaceous lavas on the attached fissure vents between 213 and 205 m (samples SV2/D16-R5 and D16-S7, supporting information Tables S1–S3, Figure 13, and supporting information Figure S6). Lapilli samples have porphyritic texture with around 5 vol % small olivine phenocrysts, and scarce, clinopyroxene phenocrysts (Figure 13b). The groundmass is fresh and glassy and the samples have up to 60 vol % vesicularity. However, unlike floated lava balloons, they do not show gradients with most of the vesicles being spherical and <0.3 mm diameter down to 0.02 mm at the smallest. Minor bubble coalescence forms larger single vesicles, but most of the bubbles preserve their spherical shape with thin bubble walls. Glassy ash are pale to dark-brown in color, formed by sideromelane glass and are elongated to fluidal-shaped with dispersed clinopyroxene crystals (supporting information Figures S4 and S6).

3.4.2.3. Scoriaceous Boulders Ejected Along the Flanks of the Principal Cone

Scoria boulders were recovered from the flanks of the principal cone (Figures (10 and 13)c, and supporting information Figure S7) at water depths of 154 (sample SV2/D16-R8, supporting information Tables S1–S3).
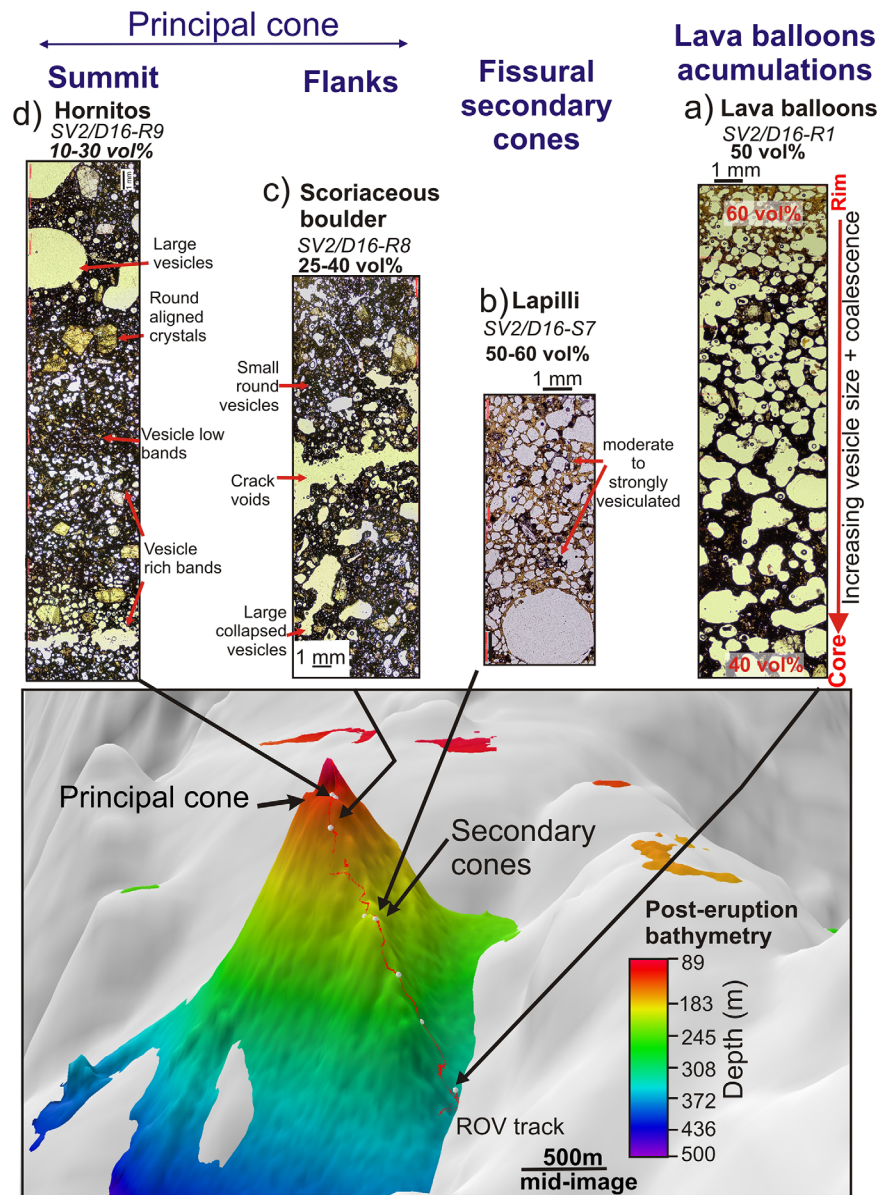
Figure 13. Images of the samples recovered by the ROV along the summit and flanks of the principal cone, secondary cones, and giant scoria deposits at the base of the Tagoro submarine volcano showing the differences in the microtextures. Sample location (white dots) and ROV track (red lines) are superimposed to the post-eruption bathymetry. (a) Agglutinated lava from the hornitos display small vesicles (0.7–1 mm) related to the banded zonation of lavas. Large rounded vesicles at the rim of the hornitos are related to hydrothermal/degasification processes. (b) Scoriaceous boulder sampled on the flank of the principal cone show large bubble collapse vesicles (>5 mm) and large fissures pointing out to explosive ejection. (c) Pyroclasts from secondary cones show spherical vesicles (0.5–3 mm) but not coalescence. (d) Lava balloon fragment shows increasing bubble size (>5 mm) and vesicles coalescence from the rim to the core. Vesicularities were determined from thin section images taken under a petrographic microscope at 50× magnification only, due to the coarsely vesicular nature of the samples [*Cashman and Mangan*, 1994].

Scoria samples have ∼25–40 vol % vesicularity and wholly crystalline groundmass, with a higher abundance of microlites than observed in the lava balloons. There are a range of vesicle sizes and shapes in the samples collected, with a population of large (0.5–5 mm) irregular bubbles that form large voids in the scoria, indicative of coalescence, along with a second population of small (<0.3 mm) spherical bubbles.

3.4.2.4. Hornito Lavas at the Summit of the Principal Cone

Fragments of lavas were recovered from the hornitos on the summit of the volcano (Figures (12 and 13)d, and supporting information Figure S8) at water depths between 114 and 90 m (samples SV2/D16-R9, D16-R12, and D16-R15, supporting information Tables S1–S3). The hornito lavas contain a crystalline

groundmass, with abundant microlites of olivine, clinopyroxene, plagioclase, and opaque minerals (Figure 13d and supporting information Figure S8). The lavas have heterogeneous texture with banded layers of low to moderately vesicular regions across mm to cm scales. Bubbles within the more vesicular regions are aligned and coalesced in a direction parallel to the banding and crystal alignment, indicative of flow, or permeability development in the lavas. In contrast, bubbles within the lower vesicularity regions are small and spherical.

4. Discussion

Studies of submarine volcanism are usually based on interpretations of seafloor or uplifted deposits long after an eruption has ceased [e.g., *Allen and McPhie*, 2009; *Conte et al.*, 2014; *Rotella et al.*, 2013]. Although such studies have provided extremely valuable information, seafloor deposits may have undergone significant sedimentation and reworking or be from multiple eruptive events of unknown duration, age, depth, or relationship [e.g., *Barker et al.*, 2012]. On the other hand, studies of active eruptions provide insights into eruptive processes directly, but are opportunistic and not as common. In such cases, discrete small-scale explosions or effusive eruptions have been documented with submersibles at arc volcanoes [e.g., *Chadwick et al.*, 2008; *Deardorff et al.*, 2011] and at mid-ocean ridges [e.g., *Embley et al.*, 1999; *Soule et al.*, 2007]. Larger eruptions have also been documented by bathymetric mapping before and after eruptions or collapse [e.g., *Wright et al.*, 2008; *Watts et al.*, 2012]. However, the rarity and inherent hazards associated with documenting larger eruptions during the event itself means there are few examples of where the eruptive sequence and its associated products are fully documented. This study provides a unique opportunity to interpret a single shallow water submarine eruption and the formation of an entirely new edifice, from the onset of eruption, allowing us to relate eruptive processes and products. Below we discuss the relationship between the changing morphology of the new Tagoro volcanic edifice and the evolution of the 2011–2012 submarine eruption based on the combination of hydroacoustic and bathymetric images taken during the eruption and submersible observations and textural-compositional features of recovered rock samples after the eruption had ceased.

4.1. Linking Observations With Deposit Types and Eruptive Activity

One of the biggest challenges in studying submarine eruptions is relating deposits with eruptive and depositional processes, especially during explosive phases. Part of the difficulty arises from the fact that pyroclastic material may be buoyant in water, with some material sinking rapidly and other material preferentially floating away from vent (e.g., highly vesicular clasts or fine grain size) [*Cashman and Fiske*, 1991]. As highlighted in this study, an additional complexity is that the growth of a new edifice may occur interspersed with periods of major collapse and mass movement, which may act to entirely cover or destroy previous deposits or any evidence for earlier activity. For example, our first survey at the end of November took place after at least two collapse events between the 25 and 29 October and between 31 October and 13 November [*Rivera et al.*, 2013]. In these collapse events the initial single cone were largely destroyed and then overprinted by mid-November by multiple vents focused northward of the initial vent (Figure 2b). We have also revealed that an additional major collapse event occurred at some point between the survey of *Rivera et al.* [2013] on 2 December and our survey on 22 December, lowering the summit of the volcano by almost 30 m, which was then once again reestablished by 11 January 2012 [*Rivera et al.*, 2013]. Notably, this collapse event coincides with a significant shift in the composition of lava balloons collected from the sea surface in early December to more primitive compositions, inferred by *Martí et al.* [2013a] to represent a magma recharge event that coincided with the partial collapse of the deeper parts of the plumbing system.

As revealed by our geochemical data, all of the samples collected by ROV are relatively restricted in composition between 7.5 and 8 wt % MgO (Figure 14), despite their range of textural features or the location in which they were collected. Both in their major and trace element characteristics, they are different to the compositions of lava balloons sampled at the sea surface between October and early November. Geochemical variations in the early floated lava balloons are interpreted to result from a combination of magma fractionation in the pre-eruptive reservoir and variable interactions between the ascending mafic magma and the layer of silica-rich oceanic sediments [*Troll et al.*, 2012; *Martí et al.*, 2013a]. Our ROV samples are instead similar to the more primitive samples collected from the sea surface from December onwards having notably higher Ni (>120 ppm), Cr (>190 ppm), V (>350 ppm), and Sc (>22 ppm) (Figure 14). We therefore
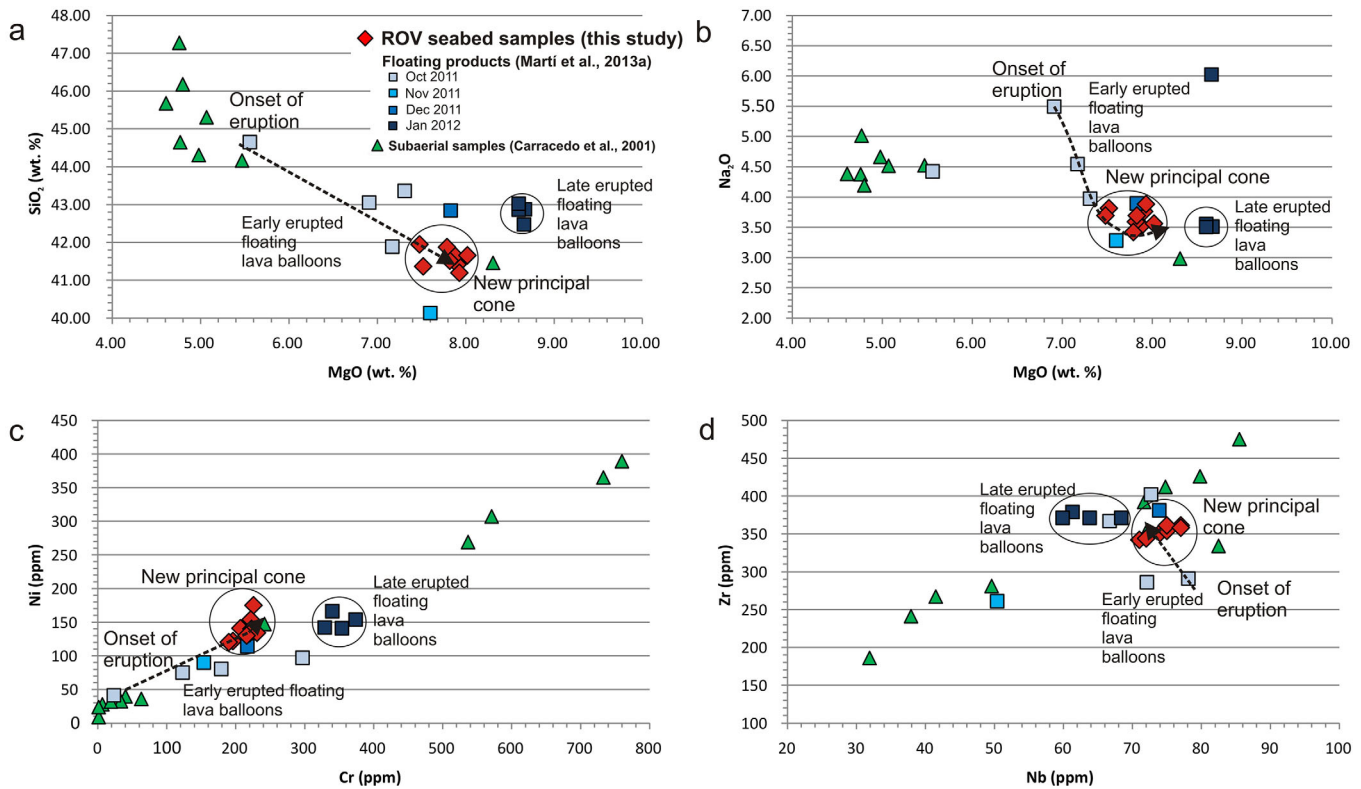
Figure 14. (a and b) Whole-rock major element variation diagrams versus wt % MgO as a differentiation index. (c) Ni versus Cr diagram, in which all samples display a fractional crystallization trend (strong negative correlation due to olivine and chromite fractionation). (d) Zr versus Nb diagram, which should show strong positive correlations for these incompatible elements as they are not fractionated by any crystallizing mineral phase (see text for explanation). Red symbols for the Tagoro seabed ROV samples collected in this study; squares symbols for *Martí et al.* [2013a] floating samples. Green symbols = basanite and tephrite samples from the different subaerial volcanic edifices in El Hierro island [*Carracedo et al.*, 2001]. All data are from whole-rock samples.

interpret that the samples collected by our ROV, and the current seafloor that makes up the proximal deposits around Tagoro, all represent material that was erupted after magma recharge and the major collapse event in early December and from the second eruptive episode, as defined by *Martí et al.* [2013a] (Figure 15). Samples collected from the sea surface in January, however, are slightly higher in MgO than our ROV samples, with notably different Nb/Zr and Cr content (Figures 14c and 14d). The differences in major element compositions observed between the *Martí et al.* [2013a] January samples and our ROV samples could mainly be due to the difference in their respective crystal content (up to 30% for the former) [*Martí et al.*, 2013a; *Longpré et al.*, 2014] and not exceeding 20% in the latter (supporting information Table S3). But differences in Nb/Zr suggest some differences in magma evolution (e.g., presence of ilmentite or clinopyroxene) or open system processes, such as magma mixing or variable incorporation of crustal sediments. As we know from the bathymetry of *Rivera et al.* [2013] that the hornitos and secondary vents we sampled formed at sometime between late January and March, this suggests that either another shift in magma chemistry occurred in late January, or that the composition of floated samples collected at the sea surface by *Martí et al.* [2013a] was not fully representative of the spectrum of magma compositions being erupted from Tagoro at this time. As our samples were collected from across the entire edifice we suggest they are most representative of the final magma composition erupted from Tagoro.

Despite the fact that the ROV recovered material has a relatively narrow compositional range and therefore represent deposits from only the second half of the eruptive episode, they still range significantly in their physical and textural characteristics (Figure 13). We attribute these variations in vesicularity to changing eruptive styles from effusive to explosive, as observed even over short time intervals in hydroacoustic images on 22 December 2011 (Figure 7). Hydroacoustic images of the plume taken in December first show a weak bent plume and lava balloons sinking to seabed. Notably, the area in which lava balloons were sinking and being deposited during this phase directly coincides with the area where lava balloons were
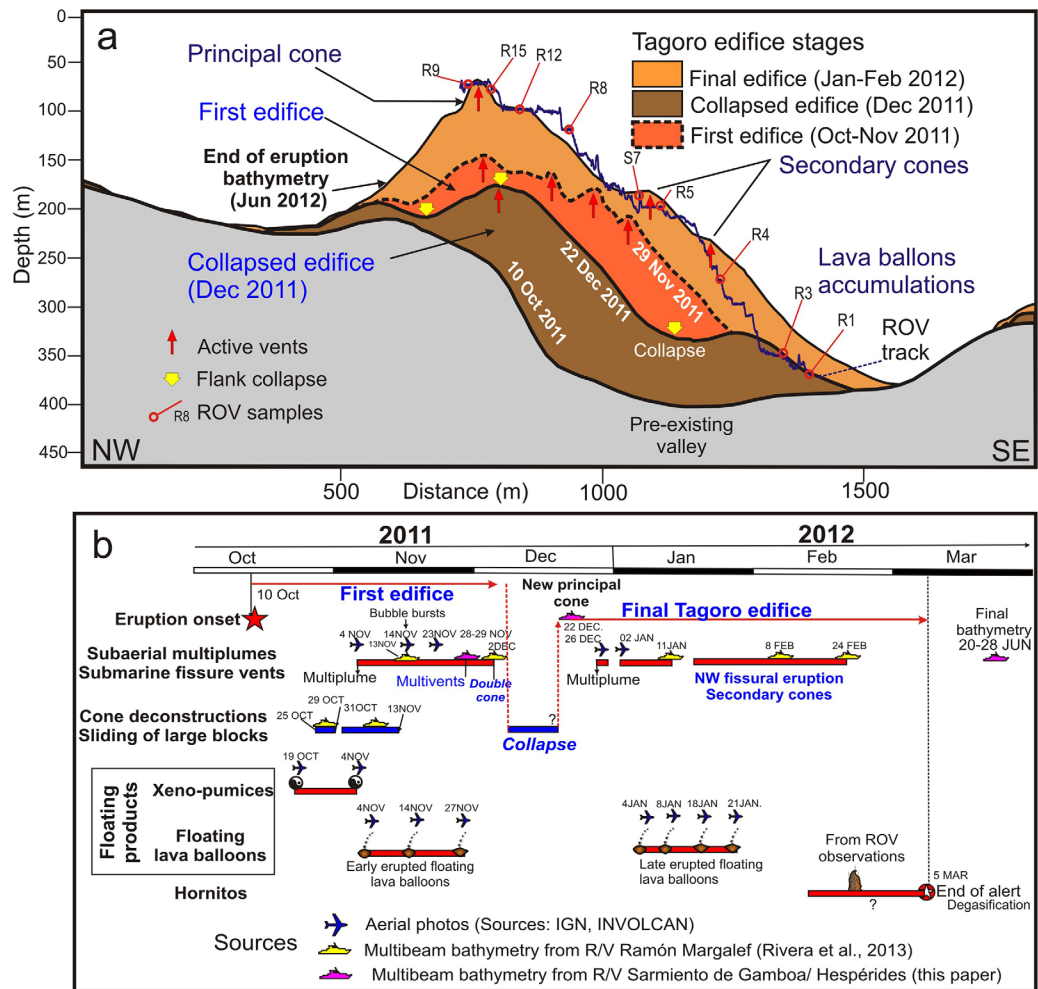
Figure 15. (a) Comparison of multibeam bathymetric profiles showing the morphological evolution of the Tagoro submarine volcano. Three main constructional-destructional phases can be differentiated. During the first phase, the Tagoro edifice was formed by multiple source vents located at 220, 195, 180, and 165 m water depths filling the pre-existing valley at 350–400 m water depth. Several collapse events of this first edifice generated a collapse of the summit of about 30 m forming a rimmed caldera and several landslides of large blocks along the flanks. After the collapse phase, a new edifice grew from 180 to 89 m water depth burying almost entirely the initial edifice. In this way, we suggest that the ROV track (blue line) and the samples collected are from the last phase of the edifice. (b) Synthesis of observations of the Tagoro eruption: morphology changes from bathymetry (combining those from *Rivera et al.* [2013] and from this paper) and products emitted and type of surface plumes from aerial photos (sources: INVOLCAN and IGN). All these data indicated that the two phases of emissions of giant buoyant vesicular products are intercalated with a period of collapse events. Based on bathymetry data, the NW fissural secondary cones were formed during the last phase. The time of formation of the hornitos is unknown, probably at the end of the eruption.

sampled later by ROV (Figure 8). As a very similar plume shape and sea surface observations were made in early November, we consider that similar stacked lava balloon deposits were being formed during these early phases of the eruption, but were largely destroyed or covered by the later collapse events. The second 22 December hydroacoustic images then show the eruption entering a more effusive stage where little or no material made it through to the sea surface, with no lava balloons observed at the surface. Only half an hour later the eruption entered a vigorous explosive phase with a strong established plume and large bubbles and upwelling observed at the surface, with large amounts of ash and fine lapilli observed at the surface and throughout the water column. This explosive phase also shows part of the column collapsing down the northern flanks of the cone to form subaqueous density currents. However, the eruption plume never breached the sea surface during this time. Similar vigorous upwelling and bubbling was observed in November (Figure 15b), indicating that explosive phases also occurred during this time. During these explosive phases the dominant material was fine ash and lapilli.

4.2. Stages of Evolution in the Formation of the New Volcanic Cone "Tagoro"

The new volcanic cone "Tagoro" formed in response several different stages of growth with changing eruptive styles throughout the event, interspersed with periods of collapse. Figure 15b integrates chronology from MBES data of our surveys from November through until June with surveys reported in *Rivera et al.* [2013] and also with those observations from aerial photos taken by the IGN and INVOLCAN (supporting information Figures S2 and S3). Here we have split the eruptive event into two main physical stages, based on the major collapse event in early-mid December, which notably closely coincides with the two eruptive episodes chosen by *Martí et al.* [2013a], based on their geophysical and petrological data. In the first eruptive episode from October until the major December collapse event, a single cone built from 10 October until early November, with a minor collapse event between 25 and 29 October [*Rivera et al.*, 2013]. In early November, a significant collapse event took place with the collapse of the southeastern valley and the main vent shifted northward with multiple vents becoming active on the southern flank as revealed by the survey of *Rivera et al.* [2013] on 13 November and our survey in late November. By the end of the first eruptive episode, a multivent edifice was built. This initial edifice largely collapsed in early to mid-December, coinciding with a distinct change in the chemistry and crystallinity of the magmas being erupted [*Martí et al.*, 2013a]. Below we describe the unique features of the El Hierro 2011–2012 eruption and describe their distinguishing features and associated products during each of these eruptive stages.

#### 4.2.1. Massive Emission of Buoyant Lava Balloons and "Xeno-Pumices"

One of the most unique features of the 2011–2012 El Hierro eruption was the occurrence of floating and steaming pyroclasts at the sea surface (Figure 5c). These peculiar "lava balloons" have also been reported from other volcanoes near Socorro Island, Mexico [*Siebe et al.*, 1995] and at Terceira, Azores [*Kueppers et al.*, 2012]. Aerial photos show that emission of floating pyroclasts on the sea surface was observed over two main periods, coinciding with the two main stages of the eruption (Figure 15b). However, in the first few months of the eruption, the type of lava balloons being erupted varied [*Troll et al.*, 2012]. From early to mid-October, until early November many of the lava balloons contained a distinct highly vesicular white pumiceous core coated in a black basanite crust (Figure 5d). Many examples also showed evidence for physical mixing between the two compositions [e.g., *Meletlidis et al.*, 2012; *Troll et al.*, 2012; *Rodríguez-Losada et al.*, 2015]. The origin and nature of these xeno-pumices have been strongly debated, with both a high-silica magma origin and sedimentary origin proposed [*Meletlidis et al.*, 2012; *Troll et al.*, 2012; *Rodríguez-Losada et al.*, 2015]. The white pumiceous material has now been shown to be of a sedimentary origin, with calcareous nanofossils proving they are sub-island Cretaceous sedimentary rocks [*Zaczek et al.*, 2015]. The sediments were partially molten and remobilized by intruding basanitic magma, causing them to vesiculate upon eruption [*Troll et al.*, 2012]. The highly vesicular nature of the xeno-pumices caused them to preferentially float in water, depending on the level of mixing between the sediments and basanite magma. Xeno-pumices were only observed in the early stages of the first eruptive phase up until early November. Their absence later in the eruption may be due to the establishment of a stable conduit which required initial clearing out of sedimentary material [*Troll et al.*, 2012]. The eruption and nature of the floating xeno-pumices can therefore be considered a function of the uniquely high volatile content of the sediments.

In contrast to the xeno-pumices, lava balloons observed from early November onward did not contain any white pumiceous material (Figure 15b). Instead, they were entirely basanitic, often exceeded 1 m in size, were sometimes hollow in their centers and many exploded at the sea surface [e.g., *Carracedo et al.*, 2015]. Lava balloons were observed at the surface at the end of the first eruptive episode (supporting information Figure S2), and during the second episode in December until late January (Figure 1b and supporting information S3). Similar features have been described for floating lava balloons in submarine basaltic eruptions at shallow depths near Socorro Island, México [*Siebe et al.*, 1995], during the 1998–2001 Serreta Submarine Ridge eruption, 10 km W Terceira Island, Azores [*Gaspar et al.*, 2003; *Kueppers et al.*, 2012] and in the 1891 submarine eruption offshore Pantelleria Island, Sicily Channel, Italy [*Carey et al.*, 2012; *Conte et al.*, 2014]. In the Socorro case, the lava clasts comprised two different types: floating scoria and reticulite. Both were proposed to form by foaming of magmatic gases (mainly CO_2) at the top of a magma chamber connected to a narrow conduit, differing in texture due to variations in the rate of eruption [*Siebe et al.*, 1995]. However, we do not observe clasts at Tagoro with such high vesicularities. At Terceira Island, lava balloons were explained by segregation and accumulation of magma gasses at low pressure on the surface of lava, leading to the development of large size bubbles (blisters) that detached from the lava and promoted lava balloon buoyant rising. In contrast, *Conte et al.* [2014] suggested that lava balloons formed in the 1891 eruption were generated during explosive

phases (equivalent to Hawaiian-type fountaining) through rapid quenching of vesicular magma and post-fragmentation bubble coalescence within the interior of the clasts. In all cases, the eruption mechanism took place at shallow depths (210–30 m water depth, Socorro Island [*Siebe et al.*, 1995]; 300–1000 m water depth, Terceira Island [*Kueppers et al.*, 2012]; ∼250 m water depth, offshore Pantelleria Island [*Conte et al.*, 2014]) and along fractures, as evidenced by progressive building of aligned cones. Such features are also similar to Tagoro, where the eruption was controlled by NW-SE fractures and developed from ca. 400 to 89 m water depth. The physical properties of the magmas erupted from Socorro and Terceira are also similar to Tagoro. Eruption temperatures determined by mineral-liquid geothermometry yielded 1030–1153°C at Tagoro [*Martí et al.*, 2013a], and 1102–1116°C at Terceira [*Kueppers et al.*, 2012]. Magma compositions, however, are different, being basanite at Tagoro and weakly alkaline basalt and trachybasalt in Terceira and Socorro, respectively [*Kueppers et al.*, 2012; *Siebe et al.*, 1995], which results in slightly different calculated viscosities at the obtained temperatures and analyzed compositions: 10^3 Pa s (Terceira) [*Kueppers et al.*, 2012] and mainly between 10^1 and 10^2 Pa s (Tagoro) [*Martí et al.*, 2013a]. *Rotella et al.* [2013] proposed that lava balloons may occur across a range of compositions up to rhyolite, and proposed that they result from an eruptive style (Tangaroan) that is unique to submarine volcanism and falls between effusive and explosive styles. Notably, lava balloons were not erupted during the most explosive phases of the El Hierro event, nor during effusive phases, as demonstrated by our hydroacoustic images in November and December (Figures 6 and 7). During the periods dominated by lava balloon emission, hydroacoustic images show a weak bent plume, with some balloons making it to the surface, but many only making it part way and then sinking. The weak plume also consists of fine ash material suggesting that the eruption is not entirely effusive in nature [e.g., *Conte et al.*, 2014]. In turn, during effusive periods, no material was observed passively detaching from the lava at vent (Figure 7). We therefore infer that lava balloon emissions occurred during periods of intermediate mass eruptive rates, and not passively from a lava lake at the vent [cf. *Kueppers et al.*, 2012], nor during highly explosive phases.

Further evidence for intermediate eruptive rates is inferred from the texture of the lava balloons collected by ROV (Figure 13). The vesicularity of the measured lava fragments grades from ∼60 vol % in the rims to <40% toward the interior of the clast, although there is notable textural variability among the deposits imaged by ROV. In a similar fashion to lapilli collected from explosive phases, the lava balloon rims are glassy and lack microlites, with small round vesicles, considered as closest to magma texture during fragmentation (Figure 13a and supporting information Figure S5). Toward the interior of the clasts, microlite abundance increases to form a crystalline groundmass, with large irregular vesicles indicating post-fragmentation vesicle coalescence, similar to samples observed at offshore Pantelleria Island [*Conte et al.*, 2014]. In the most extreme examples, the interior part of the lava balloons may be entirely hollow. We consider that such textural features and the zoning of microlites and bubble size and shape could not be formed passively from a lava lake at vent. Rather, they likely resulted from rapid quenching of buoyant fragments of vesiculating magma [e.g., *Rotella et al.*, 2013]. In such a case, the vesicular glassy surface of the balloon was rapidly quenched in water, while the interior of the balloon remained insulated, resulting in degassing, microlite growth and extensive bubble coalescence [e.g., *Conte et al.*, 2014]. This eruptive style could help explain the occurrence of lava balloons during weak plumes, as the eruption during this time was not powerful enough to explosively tear the magma apart in the conduit or establish a strong eruptive column.

As opposed to the homogeneous types of lava balloons identified during the Socorro [*Siebe et al.*, 1995] and Serreta eruptions [*Gaspar et al.*, 2003; *Kueppers et al.*, 2012], the ROV images show distinct morphologies of lava balloon deposits that change in their appearance with increasing distance from the main emission center (Figures (8 and 9), and 16). Closest to the vent, accumulations of up to 2 m giant pumice balloons dominated. With increasing distance the deposits change to ∼1 m floating amphora-like balloons and then to <1 m ellipsoidal lava balloons. It can be inferred that the observed sequence of lava balloons deposits may be caused by the difference in the ability of the particular bomb type to be transported in water and the ability of the difference sizes to float "in" or "on" the water column, before waterlogging and deposition. Only balloons with the right balance of physical properties with float in water and can be deposited over longer distances. At ∼60% vesicularity the lava will be neutrally buoyant in seawater, so any variability in vesicularity or any gas loss or water logging will result in the sinking of the clasts. Giant lava balloons near vent were neutrally buoyant blocks ejected from the emission center that were rapidly waterlogged or degassed in the water column without reaching the sea surface (Figure 16). The ROV images show lava flowing out from the inner core of the balloons (Figure 8e) indicating that the nucleus of some of the balloons were still molten when deposited
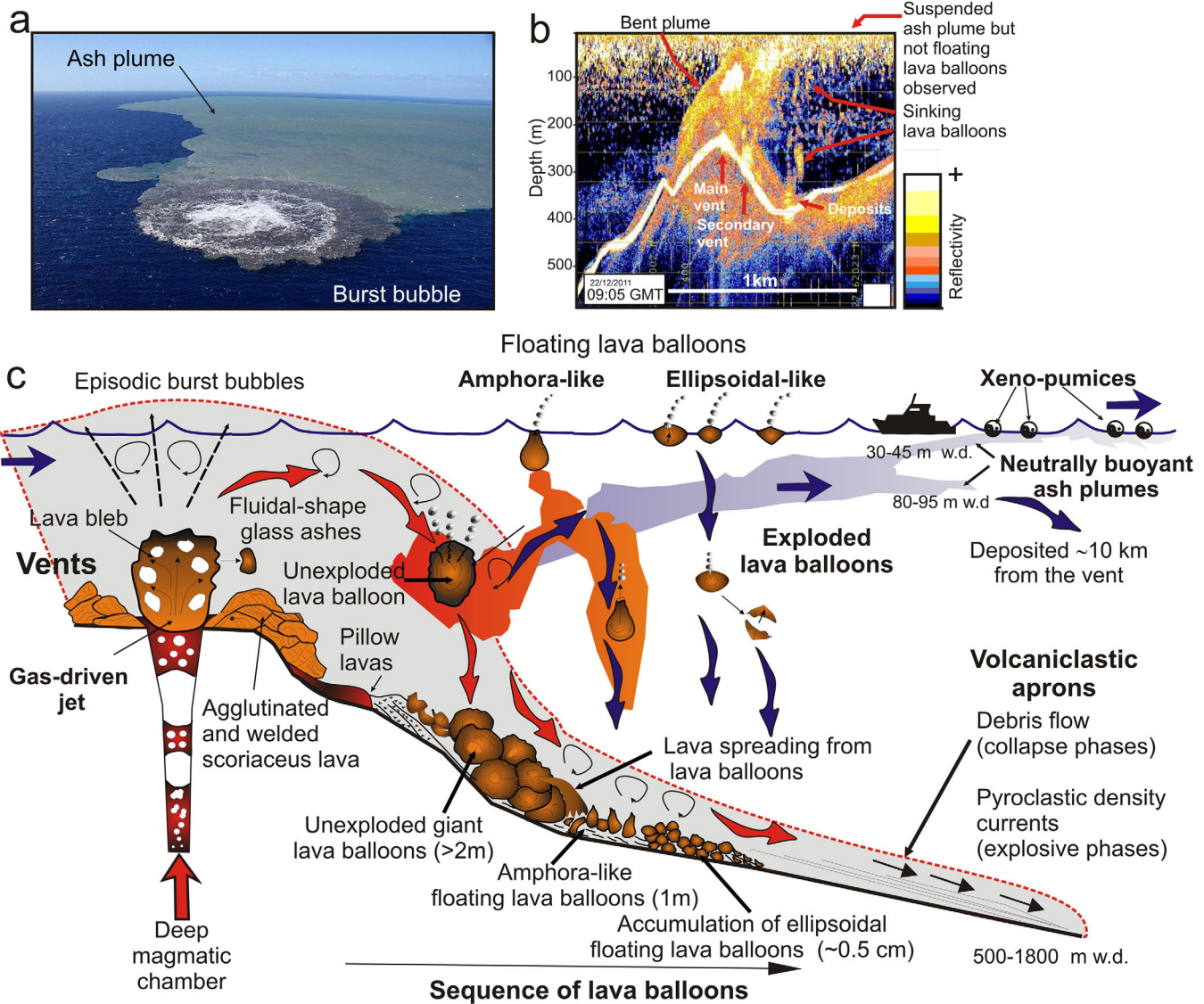
Figure 16. Synthesis of process and products during the eruption of the Tagoro volcano: (a) on the sea surface, aerial photos show bursting bubble and associated surface pyroclastic plumes (source: INVOLCAN). (b) Within the water column, high-resolution echosounder show episodic burst bubbles that emitted a gas and pyroclastic plumes from the vent to the surface and sinking giant lava vesicular blocks. (c) At the seafloor of the Tagoro volcano, ROV images showed a gradual sequence of giant buoyant vesicular lavas at the base of the Tagoro edifice as consequence of the bursting bubbles. The giant lava vesicular balloons show a sequence of gradual decreasing in size from the proximal to distal parts, i.e., (i) giant lava balloons which do not reach the sea surface (>2 m) and can be fragmented by cooling at midwaters; others can reach the seabed and split out the lava from the inner core of (ii) amphora-like balloons which reach the surface and degasificate through a vent but begin to sink before the cooling of the inner core of lava. As balloons descent to seafloor, they are molded as amphora shaped by the bottom weight but maintaining the active degassing vent at its top vertically; (iii) ellipsoidal balloons with degasification and cooling occurring both at the sea surface. The periodic explosive events cause large bubble to form at surface and generate lapilli-rich density currents which were deposited as deep-water aprons along the distal parts. In the proximal part of the vents, agglutinated and welded scoriaceous overflows rim the active vents during the late stages of the eruption.

and ruptured at the seafloor. The balloons show thick outer bread-like crusts that would act as thermal insulation during their formation, but many show evidence that this layer was breached and broken during their transport (Figure 8c), making it unlikely that they made it far from the vent. The "amphora"-like balloons show open conduits indicating that degasification took place on the sea surface, as observed during the eruption. These balloons began to sink after sufficient degassing at the sea surface such that they were no longer buoyant and the amphora shape was molded by gravitational force in the inner core during degassing and sinking of the denser interior lava (Figures 8f and 8h). In contrast, ellipsoidal balloons were smaller in size than the giant lava balloons or amphora types and reached farthest distance from vent before sinking. These were the dominant population observed at the surface during both the first and second eruptive phases and we suggest that their smaller size allowed for more effective insulation and prevention of water logging or degassing.

This type of lava balloons were often observed exploding at the sea surface as water entered cracks in their surface, resulting in multiple fragments sinking to the sea floor. Similar observations of exploding pyroclasts were made in Terceira and interpreted as explosions from magma-water interaction or from internal overpressure within the balloon [e.g., *Kueppers et al.*, 2012].

4.2.2. Edifice Collapse in Response to Changes in the Magma Reservoir

At least two episodes of collapse of the first edifice occurred between 25 October and 22 December 2011 based both on our bathymetry profiles and those published by *Rivera et al.* [2013] (Figure 15b). The first episode includes an initial collapse, between 25 and 29 October, that was attributed to emptying and subsequent failure and subsidence of a shallow magmatic chamber. A subsequent collapse shortly after, between 31 October and 13 November 2011, is associated with cone instability and sliding of a large block [*Rivera et al.*, 2013]. We identified an abrupt collapse of the first edifice to have occurred between 28 November and 22 December (Figure 15b) and estimated a decrease in height of ca. 25 m (Figure 2c), with the formation of a collapse rim. We suggest that these collapse events can be attributed to deflation of the shallow magma reservoir and recharge of a new batch of magma. *Martí et al.* [2013a] showed that the magmas erupted from 5 December were distinctly different in their geochemistry and crystallinity, being more primitive and different in their crystal content than the previously erupted magmas from the first episode. This change in composition also coincides with a change in seismicity that *Martí et al.* [2013a] interpreted as resulting from magma recharge and collapse of the shallow chamber. We extend their interpretations to suggest that the magma recharge event and the change in the structure of the magma system led to collapse of the initial edifice in early December. The recharge of magma led to heating of the remaining reservoir and a reduction in the viscosity of the erupted magmas and an overall decrease in the eruptive rate [*Martí et al.*, 2013a]. Indeed, eruptive activity in the second episode shows evidence for more effusive activity with ROV dives identifying lavas and scoria in proximal deposits around the secondary fissure cones and lavas covering earlier lava balloon deposits (Figure 9b). However, eruptive styles still varied with both explosive phases forming vesicular glassy lapilli, and also the formation of lava balloons until late January (Figure 15b), which we interpret to be a function of variable eruptive rates over short periods.

4.2.3. Volcaniclastic Deep-Water Aprons Formed by Collapse Events and High-Density Currents

During this first phase of the eruption, two aprons were deposited surrounding the principal cone at 500–850 m water depth (proximal apron) and 1000–1800 m water depth (distal apron). We estimate 19.3×10^6 NDRE m^3 in volume for the proximal apron and 39.1×10^6 NDRE m^3 for the deep fan-like apron. The formation of these aprons is driven by three dominant processes in the formation of Tagoro: debris flow, turbidites, and pyroclastic density currents. We infer that a significant volume of these aprons was produced during remobilization of volcanic products during the collapse of the edifice as observed in mid-late October and November [*Rivera et al.*, 2013] and by our survey in December. The slopes of the upper flanks of Tagoro are in the range of 25–35°, close to the equilibrium angle of repose of 30–35° for sand size material on subaqueous slopes [*Clague et al.*, 2011], so very little loading has to be added to trigger downslope movement. The comparative grid between the 22 December and the pre-eruption bathymetry shows a significant mass deficit on the southern flank with negative depth changes up −45 m (Figure 3d). This deficit of mass is interpreted as a large submarine landslide on the south flank triggered by the collapse of volcanic edifice. Therefore, we infer that the proximal apron up to 65 m in thickness was constructed mainly by flank collapse events similar to those described by *Schmincke and Segschneider* [1998] in the flanks of Gran Canary Island. Otherwise, the distal apron shows an up to 55 m thickness in its upper part and 35 m at its lower part. The fan-like shape of the distal apron resembles turbidity deposition derived from debris flows (Figure 3c). These two modes of transport, debris flow, and turbidite-derived currents also characterize the sequence of basaltic volcanoclastic aprons around the Gran Canaria Island drilled from ODP Leg 157 [*Schmincke and Sumita*, 1998]. The thickness distribution of the distal apron indicates that it has been sourced not only from the flank collapse of the volcano, but also from surrounding collapse valleys (Figure 3a). The fact that these two volcaniclastic aprons represent up to 68% of the total volume of volcanic material deposited after the collapse event points out the importance of mass-transport deposits in active volcanic eruptions. Turbiditic layers found on the flanks of NW Rota-1, Northern Mariana Islands, at depths from 700 m to more 1400 m are also related to mass-wasting events occurred during the eruption [*Embley et al.*, 2006]. Furthermore, real-time echosounder images taken after the main collapse event also suggest that submarine pyroclastic density currents may have also contributed to the volcaniclastic aprons periodically. Recent high-resolution mapping of the proximal apron suggests that it was smoothed by pyroclastic flows [*Vázquez et al.*, 2016]. Hydroacoustic images taken after the collapse

event (Figures 7c and 7d) show evidence for the formation of plumes detached from the gas-driven jet, forming downslope gravity flows [e.g., *Allen and McPhie*, 2009]. Such dense particle plumes containing shards of volcanic glass have been observed at active arc volcanoes around NW Rota-1, Northern Mariana Arc [*Embley et al.*, 2006; *Walker et al.*, 2008], West Mata, NE Lau Basin [*Embley et al.*, 2014a], South Sarigan Islands, Southern Seamount Province of Mariana arc [*Embley et al.*, 2014b], Monowai cone, Kermadec-Tonga arc [*Walker et al.*, 2010], and Kavachi volcano, Solomon Islands [*Baker et al.*, 2002].

4.2.4. Explosive Activity: Periodic Explosions and Progressive Sealing of the Vent

Explosive activity varied throughout the eruption and can be grouped into two end-member types. First, during the periods of higher eruptive rates, hydroacoustic images show the formation of a vertical eruptive column through water and the establishment of a gas-driven jet (Figure 7). We interpret these eruptions at their highest intensity to be driven by magmatic explosivity and volatile exsolution, combined with water interaction, which is supported by the abundance of vesicular glassy lapilli observed in abundance at the surface during explosive phases and then recovered during ROV sampling (Figure 11). Fluidal shapes observed in ash-sized pyroclasts (supporting information Figures S4 and S6) have been observed in submarine basaltic eruptions ranging from Strombolian to Hawaiian in eruptive styles [*Clague et al.*, 2003a, 2003b; *Conte et al.*, 2014]. These magmas are at the appropriate depth range (<200 m) at which explosions driven by magmatic volatiles may be expected to occur for such compositions [*Head and Wilson*, 2003; *Friedman et al.*, 2012]. Explosive activity of this kind was periodically observed in both the first phase and until late January during the second phase, as evidenced by large upwelling and at the sea surface and the formation of huge bursting bubbles >15 m high [*Carracedo et al.*, 2012b]. Second, along the flanks of the principal cone at ca. 120 m water depth, submersible observations identified numerous angular boulders of different sizes (often 1–2 m across) with distinctive degassed-bubble textures, high crystallinity and only 25–40 vol % vesicularity (Figures (11 and 13)c, and supporting information Figure S7). Such deposits are characterized by the dominance of angular blocks of country rocks deposits in the vicinity of a crater. We interpret that this type of deposit may result from periodic Vulcanian eruptions [*Head and Wilson*, 2003], likely triggered by late stage overpressure and gas accumulation at the top of the vent as it was progressively sealed by crystallizing magma. Further evidence for this style of eruption can be derived from the microtexture of the scoria clasts, which display abundant microlites and large irregular vesicles indicating degassing, and a second population of small vesicles that formed during their remobilization and eruption (Figure 13c and supporting information Figure S7). These deposits and the inferred eruptive style are more typical of the later part of the eruption and probably resulted from a lower or more irregular magma supply rate as the shallow reservoir became exhausted [*Martí et al.*, 2013a].

4.2.5. Effusive Activity, the Formation of "Hornitos" and Late-Stage High Temperature Geothermal Alteration

Effusive activity from the secondary cones in late January to February produced lava ponds and bulbous pillow lava flows overlying previous accumulations of more explosive products as lava balloons. This observation suggests that effusive stages post-dated the more explosive events and lava balloon emission that dominated in December and early January (Figure 15). However, some lava ponds are also covered by fluidal-shaped ash and glassy lapilli, indicating that both effusive and pyroclastic material were being produced in this late stage, but probably from multiple vents. *Resing et al.* [2011] showed that both effusive and pyroclastic material were being produced simultaneously during the summit eruptions at West Mata, i.e., the explosive degassing events also were producing degassed pillow lava flows. Such features may be the result of decreasing but variable magma supply toward the end of the eruptive event at El Hierro. In addition, effusive activity combined with hydrothermal venting is indicated by the occurrence of numerous hornitos at the summit of the principal cone (Figure 12). All the submarine hornito-like structures in Tagoro volcano share similar features with their onshore counterparts, including metric conical to cylindrical accumulations of scoriaceous lava spatter and small eruptive vents with emission of small amounts of lava fragments and degassing structures. During the final stage of eruption, the magma was driven to the surface through sheet-like ducts forming the spectacular alignment of hornitos-like structures in the summit of the underwater volcano (Figure 12). As shown in their microtextures, the hornito lavas display banded vesicles and aligned crystals indicating gas flow and permeability development (Figure 13d and supporting information Figure S8). In this setting, the formation of hornitos is interpreted as due to the interaction between lava and cold seawater producing small hydromagmatic explosions [*Hamilton et al.*, 2010]. The hot lava fragments in semifluid stage are expulsed, producing accumulation of fragments (spatter deposits) in and around the eruptive mouth to form the hornito. On land, the accumulation of gases in the lava flows could originate autoeruptions from lava flows or lava tubes as is inferred onshore in the Canary

Islands [*Araña and Carracedo*, 1978]. Once magmatic activity subsided at Tagoro, hydrothermal activity beneath the hornitos caused the water to rise at high pressure through fractures in the volcanic rocks promoting their hydrothermal alteration and the formation of Fe-oxyhydroxide precipitates and bacterial mats, that now cover the summit of the new Tagoro volcano [*González et al.*, 2017] (Figure 12f and supporting information Figure S8).

5. Conclusions

Based on an extensive array of data comprising deep-water multibeam and single-beam echo sounders, parametric chirps, remotely operated vehicle (ROV) observations, and textural and geochemical features of pyroclasts acquired along three oceanographic cruises from November 2011 to April 2014, we have outlined the evolution of eruptive activity and the products that formed a new submarine volcano in the Canary Islands, Tagoro, which grew from 375 to 89 m water depth. Our study has revealed:

1. The 2011–2012 shallow submarine eruption of El Hierro Island consisted of two main phases of construction: one from the onset of the eruption, 10 October 2011, to late November 2011 and another from December to mid-February 2012, separated by a main period of collapse of the edifice around early December 2011. The December collapse event coincided with a magma recharge and a distinct change in magma chemistry. Most volcaniclastic material generated at Tagoro volcano formed two deep-water aprons extending away from the eruptive center that make up 68% of the total volcanic material remobilized as consequence of the submarine landslides triggered by collapse events. This highlights the importance of destructive phases in the evolution of the hotspot volcanoes of the Canary Islands and how submarine cones may form over several stages of growth and collapse.

2. Eruptive activity ranged from explosive to effusive, even over short periods and therefore no single eruption style defines the formation of Tagoro. Peaks in eruption intensity during explosive phases generated vigorous bubbling at the surface with extensive ash and vesicular lapilli and formed high-density currents. Intermediate eruption rates generated weak plumes and produced lava balloons that were observed floating at the sea surface and later collected by ROV. Lava balloons range in appearance on the seafloor from proximal to distal parts, primarily as a function of their ability to float in water and be transported before waterlogging, explosion, or degassing. Effusive activity from late January produced lava ponds and generated bulbous and toothpaste-like pillows flowing downslope overlying previous accumulations of lava balloons. In the later stages of the eruption, massive accumulation of ejected country blocks suggests intermittent explosive eruptions. Numerous hornitos built up as rootless spatter cones were formed on top of Tagoro volcano in the final stages of eruption and were covered by hydrothermal S-related and Fe-related bacterial mineralization. The range of eruptive products highlights the complexity of submarine eruptions and the range of eruptive styles that may occur during their evolution.

3. Using real-time hydroacoustic monitoring during the eruption and post-eruption ROV observations, we have revealed the complexity of the El Hierro eruptive sequence and the way in which a new submarine cone is built in multiple stages of growth and collapse. Our data reinforce the importance of monitoring shallow submarine volcanoes, especially those located near to populated areas, by using a wide-range of underwater methodologies in order to better understand how such events may occur in the future.

References

Allen, S. R., and J. McPhie (2009), Products of neptunian eruptions, *Geology*, *37*(7), 639–642.
Allen, S. R., R. S. Fiske, and K. V. Cashman (2008), Quenching of steam-charged pumice: Implications for submarine pyroclastic volcanism, *Earth Planet. Sci. Lett.*, *274*, 40–49.
Araña, V., and J. C. Carracedo (1978), *Los volcanes de las Islas Canarias III. Lanzarote y Fuerteventura*, 106 pp., Ed. Rueda, Madrid, Spain.
Arculus, R. (2011), Submarine volcanism: Deeply explosive, *Nat. Geosci.*, *4*, 737–738.
Baker, E. T., G. J. Massoth, C. E. J. de Ronde, J. E. Lupton, and B. I. A. McInnes (2002), Observations and sampling of an ongoing subsurface eruption of Kavachi volcano, Solomon Islands, May 2000, *Geology*, *30*(11), 975–978.
Barker, S. J., M. D. Rotella, C. J. N. Wilson, I. C. Wright, and R. J. Wysoczanski (2012), Contrasting pyroclast density spectra from subaerial and submarine silicic eruptions in the Kermadec arc: Implications for eruptive processes and dredge sampling, *Bull. Volcanol.*, *74*, 1425–1443.
Barker, S. J., C. J. N. Wilson, J. A. Baker, M.-A. Millet, M. D. Rotella, I. C. Wright, and R. J. Wysoczanski (2013), Geochemistry and petrogenesis of silicic magmas in the intra-oceanic Kermadec arc, *J. Petrol.*, *54*(2), 351–391.
Becerril, L., I. Galindo, A. Gudmundsson, and J. M. Morales (2013), Depth of origin of magma in eruptions, *Nat. Sci. Rep.*, *3*, 2762, doi:10.1038/srep02762.
Binard, N., R. Hékinan, J. L. Cheminée, and P. Stoffers (1992), Styles of eruptive activity on intraplate volcanoes in the Society and Austral hot spot regions: Bathymetry, petrology, and submersible observations, *J. Geophys. Res.*, *97*, 13,999–14,015.

Carey, S. N., K. L. C. Bell, M. Marani, M. Rosi, E. T. Baker, C. Roman, M. Pistolesi, and T. J. Kelly (2012), Submarine volcanism in the Strait of Sicily, *Oceanography*, *25*(1), 34–35.

Carracedo, J. C., E. R. Badiola, H. Guillou, J. de la Nuez, and J. F. Pérez Torrado (2001), Geology and volcanology of La Palma and El Hierro, Western Canaries, *Est. Geol.*, *57*, 175–273.

Carracedo, J. C., J. F. Pérez Torrado, A. Rodríguez González, V. Soler, J. L. Fernández Turiel, A. Klügel, V. R. Troll, and S. Wiesmaier (2012a), The ongoing volcanic eruption of El Hierro, Canary Islands, *Eos Trans. AGU*, *93*, 89–90.

Carracedo, J. C., J. F. Pérez Torrado, A. Rodríguez González, V. Soler, J. L. Fernández Turiel, V. R. Troll, and S. Wiesmaier (2012b), The 2011 submarine volcanic eruption in El Hierro (Canary Islands), *Geol. Today*, *28*(2), 53–58.

Carracedo, J. C., V. R. Troll, K. Zaczek, A. Rodríguez-González, V. Soler, and F. M. Deegan (2015), The 2011–2012 submarine eruption off El Hierro, Canary Islands: New lessons in oceanic island growth and volcanic crisis management, *Earth Sci. Rev.*, *150*, 168–200.

Cashman, K. V., and R. S. Fiske (1991), Fallout of pyroclastic debris from submarine volcanic eruptions, *Science*, *253*(5017), 275–280.

Cashman, K. V., and M. T. Mangan (1994), Physical aspects of magmatic degassing II. Constraints on vesiculation processes from textural studies of eruptive products, *Rev. Mineral. Geochem.*, *30*, 447–478.

Chadwick, W. W. Jr., K. V. Cashman, R. W. Embley, H. Matsumoto, R. P. Dziak, C. E. J. de Ronde, T.-K. Lau, N. Deardorff, and S. G. Merle (2008), Direct video and hydrophone observations of submarine explosive eruptions at NW Rota-1 Volcano, Mariana Arc, *J. Geophys. Res.*, *113*, B08S10.

Clague, D. A., R. Batiza, J. Head, and A. S. Davis (2003a), Pyroclastic and hydroclastic deposits on Loihi Seamount, Hawaii, in *Explosive Sub-aqueous Volcanism*, edited by J. D. L. White et al., pp. 73–95, AGU, Washington, D. C.

Clague, D. A., A. S. Davis, and J. E. Dixon (2003b), Submarine Strombolian eruptions along the Gorda mid-ocean ridge, in *Explosive Subaque-ous Volcanism*, edited by J. D. L. White et al., pp. 111–128, AGU, Washington, D. C.

Clague, D. A., J. B. Paduan, D. W. Caress, H. Thomas, W. W. Chadwick Jr., and S. G. Merle (2011), Volcanic morphology of West Mata Volcano, NE Lau Basin, based on high-resolution bathymetry and depth changes, Geochem. *Geophys. Geosyst.*, *12*, QOAF03, doi:10.1029/2011GC003791.

Conte, A. M., E. Martorelli, M. Calarco, A. Sposato, C. Perinelli, M. Coltelli, and F. L. Chiocci (2014), The 1891 submarine eruption offshore Pantelleria Island (Sicily Channel, Italy): Identification of the vent and characterization of products and eruptive style, *Geochem. Geophys. Geosyst.*, *15*, 2555–2574, doi:10.1002/2014GC005238.

Deardorff, N. D., K. V. Cashman, and W. W. Chadwick Jr. (2011), Observations of eruptive plume dynamics and pyroclastic deposits from submarine explosive eruptions at NW Rota-1, Mariana arc, *J. Volcanol. Geotherm. Res.*, *202*, 47–59.

Embley, R. W., W. W. Chadwick, D. Clague, and D. Stakes (1999), 1998 eruption of axial volcano: Multibeam anomalies and seafloor observations, *Geophys. Res. Lett.*, *26*, 3425–3428.

Embley, R. W., et al. (2006), Long-term eruptive activity at a submarine arc volcano, *Nature*, *441*, 494–497.

Embley, R. W., et al. (2014a), Eruptive modes and hiatus of volcanism at West Mata seamount, NE Lau basin: 1996–2012, *Geochem. Geophys. Geosyst.*, *15*, 4093–4115, doi:10.1002/2014GC005387.

Embley, R. W., Y. Tamura, S. G. Merle, T. Sato, O. Ishizuka, W. W. Chadwick Jr., D. A. Wiens, P. Shore, and R. J. Stern (2014b), Eruption of South Sarigan Seamount, Northern Mariana Islands: Insights into hazards from submarine volcanic eruptions, *Oceanography*, *27*(2), 24–31.

Eugenio, F., J. Martin, J. Marcello, and E. Fraile-Nuez (2014), Environmental monitoring of El Hierro Island submarine volcano, by combining low and high resolution satellite imagery, *Int. J. Appl. Earth Obs. Geoinf.*, *29*, 53–66.

Fiske, R. S., K. V. Cashman, A. Shibata, and K. Watanabe (1998), Tephra dispersal from Myojinsho, Japan, during its shallow submarine eruption of 1952–1953, *Bull. Volcanol.*, *59*, 262–275.

Friedman, P. D., S. Carey, and M. Raessi (2012), Influence of volatile degassing on initial flow structure and entrainment during undersea volcanic fire fountaining eruptions, *Nat. Sci.*, *4*(12), 1002–1012, doi:10.4236/ns.2012.412129.

Fouquet, Y., J. Eissen, H. Ondreas, F. Barriga, R. Batiza, and L. Danyushevsky (1998), Extensive volcaniclastic deposits at the Mid-Atlantic Ridge axis: Results of deep-water basaltic explosive volcanic activity?, *Terra Nova*, *10*(5), 280–286.

Gaspar, J. L., G. Queiroz, J. M. Pacheco, T. Ferreira, N. Wallenstein, M. H. Almeida, and R. Coutinho (2003), Basaltic lava balloons produced during the 1998–2001 Serreta Submarine Ridge eruption (Azores), in *Explosive Subaqueous Volcanism, Geophys. Monogr. AGU*, 140, 205–212.

González, F. J., B. Rincón-Tomás, L. Somoza, J. R. Hein, T. Medialdea, P. Madureira, J. Reyes, M. Hoppert, and J. Reitner (2017), Fe-rich miner-alized microbes from hydrothermal vents at Tagoro submarine volcano, El Hierro Island (central east Atlantic), Geological Society of America, 113th Annual Meeting, vol. 49, 4 pp., Hawaii, doi:10.1130/abs/2017CD-292519.

González, P. J., S. V. Samsonov, S. Pepe, K. F. Tiampo, P. Tizzani, F. Casu, J. Fernandez, A. G. Camacho, and E. Sansosti (2013), Magma storage and migration associated with the 2011–2012 El Hierro eruption: Implications for crustal magmatic systems at oceanic island volcanoes, *J. Geophys. Res. Solid Earth*, *118*, 4361–4377, doi:10.1002/jgrb.50289.

Guillou, H., J. C. Carracedo, F. J. Pérez-Torrado, and E. Rodríguez Badiola (1996), K-Ar ages and magnetic stratigraphy of a hotspot-induced, fast grown oceanic island: El Hierro, Canary Islands, *J. Volcanol. Geotherm. Res.*, *73*, 141–155.

Hamilton, C. W., T. Thordarson, and S. A. Fagents (2010), Explosive lava-water interactions I: Architecture and emplacement chronology of volcanic rootless cone groups in the 1783–1784 Laki lava flow, Iceland, *Bull. Volcanol.*, *72*, 449–467.

Head, III, J. W., and L. Wilson (2003), Deep submarine pyroclastic eruptions: Theory and predicted landforms and deposits, *J. Volcanol. Geotherm. Res.*, *121*, 155–193.

Ibáñez, J. M., S. De Angelis, A. Díaz-Moreno, P. Hernández, G. Alguacil, A. Posadas, and N. Pérez (2012), Insights into the 2011–2012 submarine eruption off the coast of El Hierro (Canary Islands, Spain) from statistical analyses of earthquake activity, *Geophys. J. Int.*, *191*, 659–670.

Jurado-Chichay, Z., S. K. Rowland, and G. P. Walker (1996), The formation of circular littoral cones from tube-fed pāhoehoe: Mauna Loa, Hawaii, *Bull. Volcanol.*, *57*(7), 471–482.

Kueppers, U., A. R. Nichols, V. Zanon, M. Potuzak, and J. M. Pacheco (2012), Lava balloons-peculiar products of basaltic submarine eruptions, *Bull. Volcanol.*, *74*(6), 1379–1393.

Le Maitre, R. W., et al. (1989), *A Classification of Igneous Rocks and Glossary of Terms: Recommendations of the International Union of Geological Sciences Subcommission on the Systematics of Igneous Rocks*, 193 pp., Blackwell Sci., Oxford, U. K.

Longpré, M.-A., A. Klügel, A. Diehl, and J. Stix (2014), Mixing in mantle magma reservoirs prior to and during the 2011–2012 eruption at El Hierro, Canary Islands, *Geology*, *42*, 311–314.

López, C., et al. (2012), Monitoring the volcanic unrest of El Hierro (Canary Islands) before the onset of the 2011–2012 submarine eruption, *Geophys. Res. Lett.*, *39*, L13303, doi:10.1029/2012GL051846.

Martí, J., A. Castro, C. Rodríguez, F. Costa, S. Carrasquilla, R. Pedreira, and X. Bolos (2013a), Correlation of magma evolution and geophysical monitoring during the 2011–2012 El Hierro (Canary Islands) submarine eruption, *J. Petrol.*, *54*, 1349–1373.

Martí, J., V. Pinel, C. López, A. Geyer, R. Abella, M. Tárraga, M. J. Blanco, A. Castro, and C. Rodríguez (2013b), Causes and mechanisms of the 2011–2012 El Hierro (Canary Islands) submarine eruption, *J. Geophys. Res. Solid Earth*, *118*, 823–839, doi:10.1002/jgrb.50087.

Martínez-Frías J., J. A. Rodríguez-Losada, F. Rull, and A. Eff-Darwich (2012), The pumice-like unusual pyroclasts from El Hierro submarine eruption (Canary Islands): Hydrothermal signature, new genetic insights and astrobiological significance, Abstract Book 34th International Geological Congress (IGC), Australia.

Meletlidis, S., A. Di Roberto, M. Pompilio, A. Bertagnini, I. Iribarren, A. Felpeto, P. A. Torres, and C. D'Oriano (2012), Xenopumices from the 2011–2012 submarine eruption of El Hierro (Canary Islands, Spain): Constraints on the plumbing system and magma ascent, *Geophys. Res. Lett.*, *39*, L17302, doi:10.1029/2012GL052675.

Murtagh, R. M., and J. D. L. White (2013), Pyroclast characteristics of a subaqueous to emergent Surtseyan eruption, Black Point volcano, California, *J. Volcanol. Geotherm. Res.*, *267*, 75–91, doi:10.1016/j.jvolgeores.2013.08.015.

Pellicer, M. J. (1977), Estudio volcanológico de la isla de El Hierro, Islas Canarias, *Est. Geol.*, *33*, 181–197.

Pérez, N. M., G. Padilla, E. Padrón, P. A. Hernández, G. Melián, J. Barrancos, S. Dionis, D. Nolasco, F. Rodríguez, D. Calvo, and I. Hernández (2012), Precursory diffuse CO_2 and H_2S emission signatures of the 2011–2012 El Hierro submarine eruption, Canary Islands, *Geophys. Res. Lett.*, *39*, L16311, doi:10.1029/2012GL052410.

Pérez, N. M., et al. (2014), Evidence from acoustic imaging for submarine volcanic activity in 2012 off the west coast of El Hierro (Canary Islands, Spain)), *Bull. Volcanol.*, *76*, 882–896.

Pérez-Torrado, F. J., J. C. Carracedo, A. Rodríguez-Gonzalez, V. Soler, V. R. Troll, and S. Wiesmaier (2012), La erupción submarina de La Restinga en la isla de El Hierro, Canarias: Octubre 2011-Marzo 2012, *Est. Geol.*, *68*(1), 5–27.

Resing, J. A., et al. (2011), Active submarine eruption of boninite in the northeastern Lau Basin, *Nat. Geosci.*, *4*, 799–806, doi:10.1038/ngeo1275.

Rodríguez-Losada, J. A., A. Eff-Darwich, L. E. Hernández, R. Viñas, N. Pérez, P. Hernández, G. Melián, J. Martínez-Frías, M. C. Romero-Ruiz, and J. J. Coello-Bravo (2015), Petrological and geochemical highlights in the floating fragments of the October 2011 submarine eruption offshore El Hierro (Canary Islands): Relevance of submarine hydrothermal processes, *Afr. Earth Sci.*, *102*, 41–49, doi:10.1016/j.jafrearsci.2014.11.005.

Rivera, J., G. Lastras, M. Canals, J. Acosta, B. Arrese, N. Hermida, A. Micallef, O. Tello, and D. Amblas (2013), Construction of an oceanic island: Insights from the El Hierro (Canary Islands) 2011–2012 submarine volcanic eruption, *Geology*, *41*(3), 355–358.

Rivera, J., N. Hermida, B. Arrese, D. González-Aller, J. L. Sánchez de Lamadrid, D. Gutiérrez de la Flor, and J. Acosta (2014), Bathymetry of a new-born submarine volcano: El Hierro, Canary Islands, *J. Maps*, *10*(1), 82–89.

Rotella M. D., C. J. N Wilson, S. J. Barker, and I. C. Wright (2013), Highly vesicular pumice generated by buoyant detachment of magma in subaqueous volcanism, *Nat. Geosci.*, *6*, 129–132.

Rubin, K. H., S. A. Soule, W. W. Chadwick Jr., D. J. Fornari, D. A. Clague, R. W. Embley, E. T. Baker, M. R. Perfit, D. W. Caress, and R. P. Dziak (2012), Volcanic eruptions in the deep sea, *Oceanography*, *25*(1), 142–157.

Schipper, I. C., J. D. L. White, B. F. Houghton, N. Shimizu, and R. B. Stewart (2010a), ''Poseidic'' explosive eruptions at Loihi Seamount, Hawaii, *Geology*, *38*, 291–294.

Schipper, C. I., J. D. L. White, B. F. Houghton, N. Shimizu, and R. B. Stewart (2010b), Explosive submarine eruptions driven by volatile-coupled degassing at Loihi Seamount, Hawaii, *Earth Planet. Sci. Lett.*, *295*(3–4), 497–510.

Schipper, C. I., J. D. L. White, and B. F. Houghton (2011), Textural, geochemical, and volatile evidence for a Strombolian-like eruption sequence at Loihi Seamount, Hawaii, *J. Volcanol. Geotherm. Res.*, *207*(1–2), 16–32.

Schmincke, H.-U., and B. Segschneider (1998), Shallow submarine to emergent basaltic shield volcanism of Gran Canaria: Evidence from drilling into the volcanic apron, in Proc. Ocean Drill. Program Sci. Results, edited by P. P. E. Weaver et al., vol. 157, pp. 141–181, Ocean Drilling Program, College Station, Tex., doi:10.2973/odp.proc.sr.157.110.1998.

Schmincke, H.-U., and M. Sumita (1998), Volcanic evolution of Gran Canaria reconstructed from apron sediments: Synthesis of VICAP project drilling, in *Proc. Ocean Drill. Program Sci. Results*, edited by P. P. E. Weaver et al., vol. 157, pp. 443–469, Ocean Drilling Program, College Station, Tex., doi:10.2973/odp.proc.sr.157.135.1998.

Siebe, C., J. C. Komorowski, C. Navarro, J. McHone, H. Delgado, and A. Cortés (1995), Submarine eruption near Socorro Island, Mexico: Geochemistry and scanning electron microscopy studies of floating scoria and reticulate, *J. Volcanol. Geotherm. Res.*, *68*, 239–271.

Somoza, L., J. Martínez-Frías, J. L. Smellie, J. Rey, and A. Maestro (2004), Evidence for hydrothermal venting and sediment volcanism discharged after recent short-lived volcanic eruptions at Deception Island, Bransfeld Strait, Antarctica, *Mar. Geol.*, *203*, 119–140.

Somoza, L., et al. (2012), Geophysical and hydroacoustic study of the active submarine volcanism in the El Hierro Island (Canarian Archipelago), *Geo-Temas*, *13*, 601–605.

Soule, S. A., D. J. Fornari, M. R. Perfit, and K. H. Rubin (2007), New insights into mid-ocean ridge volcanic processes from the 2005–2006 eruption of the East Pacific Rise, 9 46′N–9 56′N, *Geology*, *35*(12), 1079–1082.

Stern, R. J., Y. Tamura, R. W. Embley, O. Ishizuka, S. G. Merle, N. K. Basu, and S. H. Bloomer (2008), Evolution of West Rota Volcano, an extinct submarine volcano in the southern Mariana Arc: Evidence from sea floor morphology, remotely operated vehicle observations and $^{40}Ar–^{39}Ar$ geochronological studies, *Isl. Arc*, *17*(1), 70–89.

Thordarson, T., and A. Hoskuldsson (2002), Iceland, in *Classic Geology in Europe 3*, Terra Publ., Hertfordshire, England.

Troll, V. R., et al. (2012), Floating stones off El Hierro, Canary Islands: Xenoliths of preisland sedimentary origin in the early products of the October 2011 eruption, *Solid Earth*, *3*, 97–110.

Vázquez, J. T., et al. (2016), Preliminary geomorphological analysis of the Tagoro Volcano underwater eruption (submarine slope of El Hierro Island), Abstract Book V Simposio Internacional de Ciencias del Mar, Universidad de Alicante, Alicante, Spain.

Walker, S. L., E. T. Baker, J. A. Resing, W. W. Chadwick Jr., G. T. Lebon, J. E. Lupton, and S. G. Merle (2008), Eruption-fed particle plumes and volcaniclastic deposits at a submarine volcano: NW Rota-1, Mariana Arc, *J. Geophys. Res.*, *113*, B08S11, doi:10.1029/2007JB005441.

Walker, S. L., E. T. Baker, M. I. Leybourne, C. E. J. de Ronde, R. Greene, K. Faure, W. W. Chadwick, R. P. Dziak, J. E. Lupton, and G. Lebon (2010), Transport of fine ash through the water column at erupting volcanoes—Monowai cone, Kermadec-Tonga Arc, Abstract T13B2193 presented at 2010 Fall Meeting, AGU, San Francisco, Calif., 13–17 Dec.

Watts, A. B., C. Peirce, I. Grevemeyer, M. Paulatto, W. Stratford, D. Bassett, J. A. Hunter, L. M. Kalnins, and C. E. J. de Ronde (2012), Rapid rates of growth and collapse of Monowai submarine volcano, Kermadec Arc, *Nat. Geosci.*, *5*, 510–515, doi:10.1038/ngeo1473.

White, J. D. L., J. L. Smellie, and D. A. Clague (2003), Introduction: A deductive outline and topical overview of subaqueous explosive volcanism, in *Explosive Subaqueous Volcanism*, edited by J. D. L. White et al., pp. 1–20, AGU, Washington, D. C.

Wright, I. C., W. W. Chadwick Jr., C. E. J. D. Ronde, D. Reymond, O. Hyvernaud, H.-H. Gennerich, P. Stoffers, K. Mackay, M. Dunkin, and S. C. Bannister (2008), Collapse and reconstruction of Monowai submarine volcano, Kermadec arc, 1998–2004, *J. Geophys. Res.*, *113*, B08S03, doi:10.1029/2007JB005138.

Zaczek, K., V. R. Troll, M. Cachao, J. Ferreira, F. M. Deegan, J. C. Carracedo, V. Soler, F. C. Meade, and S. Burchardt (2015), Nannofossils in 2011 El Hierro eruptive products reinstate plume model for Canary Islands, *Nat. Sci. Rep.*, *5*, 7945.